In presenting this dissertation in partial fulfillment of the requirements for an advanced degree at Idaho State University, I agree that the Library shall make it freely available for inspection. I further state that permission for extensive copying of my dissertation for scholarly purposes may be granted by the Dean of the Graduate School, Dean of my academic division, or by the University Librarian. It is understood that any copying or publication of this dissertation for financial gain shall not be allowed without my written permission.

Signature _____

Date _____

POSITRON PRODUCTION EFFICIENCY STUDY USING

HIGH REPETITION RATE LINAC AT IAC

by

Sadiq Setiniyaz

(Shadike Saitiniyazi)

A dissertation

submitted in partial fulfillment

of the requirements for the degree of

Doctor of Philosophy in the Department of Physics

Idaho State University

Jul 2013

To the Graduate Faculty:

The members of the committee appointed to examine the dissertation of Sadiq Setiniyaz (Shadike Saitiniyazi) find it satisfactory and recommend that it be accepted.

Tony Forest, Ph.D.

Major Advisor

Yujong Kim, Ph.D.

Committee Member

Dustin McNulty, Ph.D.

Committee Member

Mahbub A. Khandaker, Ph.D.

Committee Member

Wenxiang Zhu, Ph.D.

Committee Member

Acknowledgments

Thanks to my advisor Dr. Forest, who made this whole work possible. He always help me to the very details of my work patiently.

Thanks to Dr. Kim. He helped and directed me a lot on accelerator physics area of my research and experiments.

Thanks to Dr. Chouffani and Dr. Freyberger for their advise and direction in the experiments.

Thanks to engineers at IAC, especially Chad, Kevin, Brian.

Thanks to my friends Oleksiy, Jason, Mayir, Carlos, Zaijing, Olga, and Misha always there when I needed them, like lifting heavy stuff, lead bricks.

Also Thanks to my friends Chris, Jack, Tony, and many others.

Contents

List of Figures

List of Tables

Abstract

Positrons were produced using a tungsten target when impinged by an electron beam from the High Repetition Rate Linac (HRRL) at Idaho State University's (ISU) Idaho Accelerator Center (IAC). To measure the intensity of positrons at five (1-5 MeV) different energies, two dipoles were used to bend positrons to the second tungsten target where they annihilate and create 511 keV photons. 511 keV photons were measured using two NaI detectors placed horizontally and operated in coincidence. The positron beam creation and loss are explained with simulations using G4beamline. The simulation results are compared with the experiment. Although positron distribution in both simulation and experiment peaked at 3 MeV, the simulation predicted higher counts than the experiment.

= Text = ==Introduction==

Chapter 1

Introduction

1.1 Positron Beam

Positrons are used in several disciplines of sciences, like chemistry, physics, material science, surface science, biology and nanoscience [1]. Different approaches are used to generate positrons. The main challenge is increasing the intensity (or current) of the positron beam. One of the most common methods used to generate a positron beam is using an electron linac. The electron beam produces a positron beam by bremsstrahlung and pair production. One of the advantages of the linac based positrons is its variable energy and intensity.

1.1.1 Positron Beam for Positron Annihilation Spectroscopy

Positron annihilation spectroscopy is a non-damaging technique to detect defects in materials. It is based on the fact that positrons tend to annihilate near defects in the material [2]. Different depths of the materials can be probed by using variable energy positron source and a linac based variable energy positron source may be used for this purpose.

1.1.2 Positron Beam for Measuring The Impact of Two Photon Exchange

The nucleon electromagnetic form factors are fundamental quantities that are related to the charge and magnetization distribution in the nucleon. Conventionally, the nucleon form factors are measured using the Rosenbluth Technique (RT) [3]. The form factor scaling ratio, $R = \mu_p G_{Ep}/G_{Mp}$, is measured using this technique is around unity as shown in the
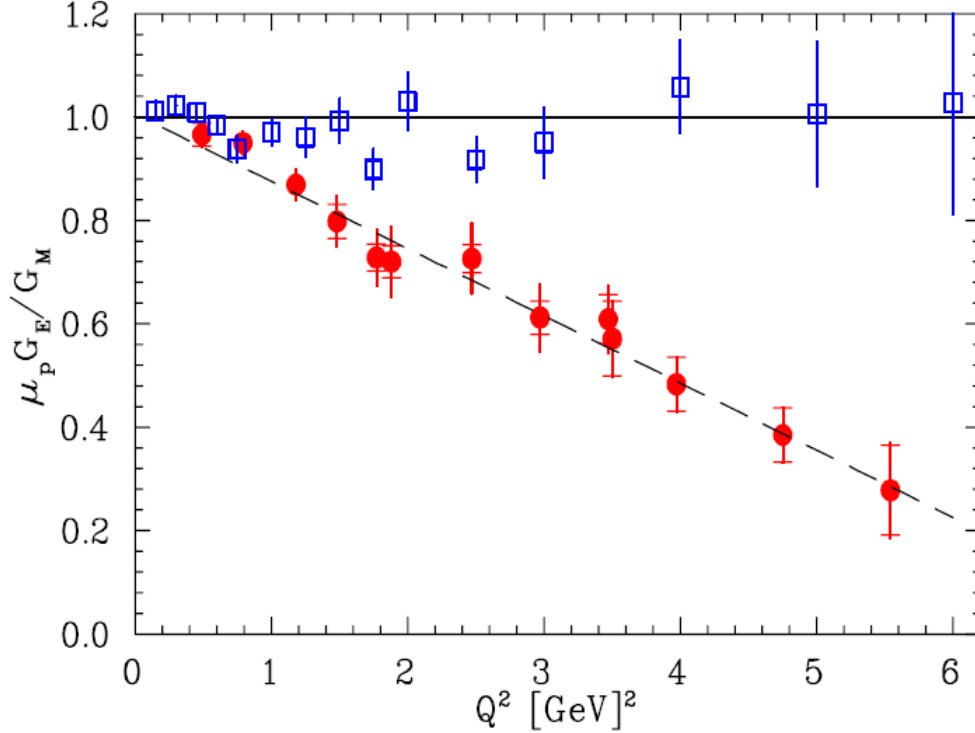
Figure 1.1: Form factor ratio, obtained by Rosenbluth Technique (hollow square) and results from Recoil Polarization Technique [5].

Fig. 1.1 [4]. Since the 1990's, a technique using elastic electron-proton polarization transfer to measure this ratio has been developed [4–6]. In this technique, form factor scaling ratio linearly decreases as the Q^2 increases, as shown in the Fig. 1.1.

The disagreement could arise from the fact that the Rosenbluth Techqniue assumes that only One Photon Exchange (OPE) occurs during the scattering while the Two Photon Exchange (TPE), which depends weakly on Q^2, could also become considerable with increasing Q^2 [5]. The contribution of TPE can be obtained by comparing the ratio of e^+ p to e^- p scattering. The interference of OPE and TPE can also be studied in the scattering process $e^+e^- \rightarrow p\bar{p}$.
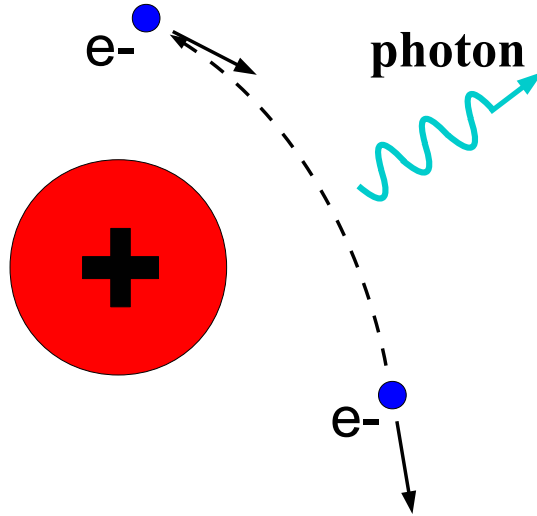
Figure 1.2: Photon generation from bremsstrahlung processes.

1.2 Positron Beam Generation from Bremsstrahlung

When a moving charged particle interacts with the electric field of another charged particle, it can be deflected and lose energy in the form of photons, as shown in the Fig. 1.2. This interaction is known as the Bremsstrahlung process. The probability of this interaction increases with the atomic number of the material traversed by the incident charged particle. Fig. 1.3 shows the photon energy distribution produced when the 12 MeV electron energy distribution from Fig. 1.4 interacts with a 1 mm thick tungsten target. As shown in the Fig. 1.3, the distribution peaks at 0.3 MeV. As the photon energy increases the number of photons produced decreases.

The bremsstrahlung cross section given is by [7]

$$d\sigma = 4Z^2 r_e^2 \alpha \frac{d\nu}{\nu} \left\{ \left(1 + \left(\frac{E}{E_0} \right)^2 \right) \left[\frac{\phi_1(\gamma)}{4} - \frac{1}{3} \ln Z - f(Z) \right] - \frac{2E}{3E_0} \left[\frac{\phi_2(\gamma)}{4} - \frac{1}{3} \ln Z - f(Z) \right] \right\},$$

$$(1.1)$$
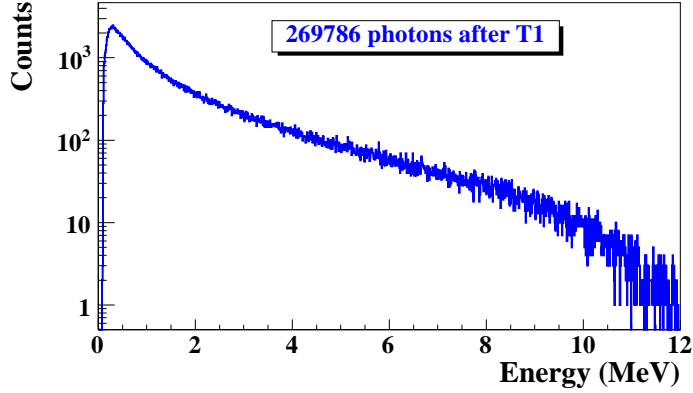
Figure 1.3: Bremsstrahlung photon energy right after a tungsten foil in simulation.

where E_0 is initial total energy of the electron, E is final total energy of the electron, $\nu = \frac{E_0 - E}{h}$ is energy of the emitted photon, and Z is atomic number of the target. $\gamma = \frac{100 m_e c^2 h \nu}{E_0 E Z^{1/3}}$ is charge screening parameter and $f(Z)$ is given by

$$f(Z) = (Z\alpha)^2 \sum_{1}^{\infty} \frac{1}{n[n^2 + (Z\alpha)^2]}, \tag{1.2}$$

where $\alpha = \frac{1}{137}$ is fine-structure constant, ϕ_1 and ϕ_2 are screening functions that depend on Z.

There are three competing processes that a photon can undergo when interacting with matter. At electron volt (eV) energies comparable to the electron atomic binding energy, the dominant photon interaction is via the photoelectric effect. As the photon energy increases up to kilo electron volt (keV) range, the Compton scattering process starts to be more dominant. Although the photon is totally absorbed during the photoelectric effect, photons merely lose energy when undergoing Compton scattering. As the photon energy reaches twice the rest mass energy of the electron, *i.e.* 2×511 keV, pair production begins to occur. Pair production becomes the dominant interaction process when photon energies are beyond 5 MeV [8]. In this process, a photon interacts with the electric field of the nucleus or the bound electrons and is converted into an electron and positron pair.

5
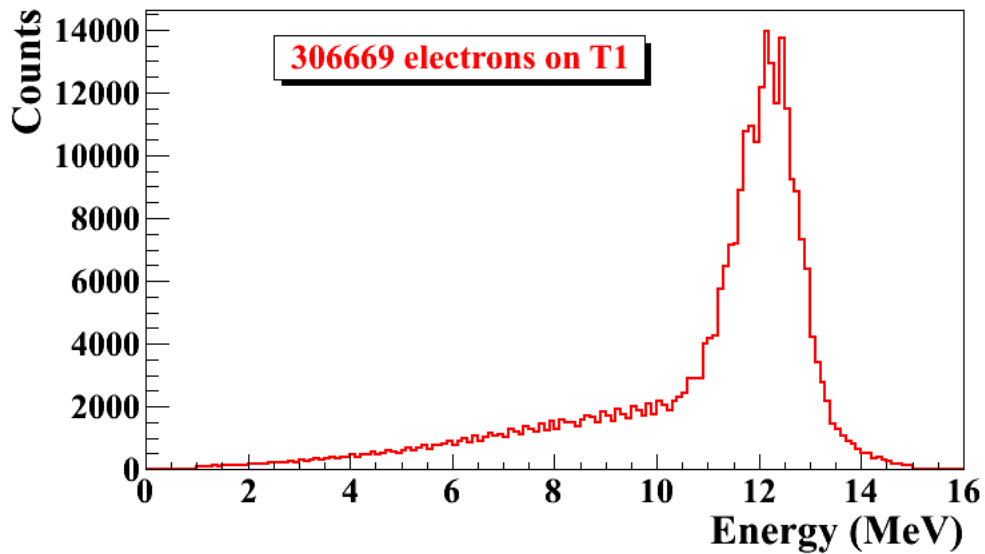
Figure 1.4: The electron energy distribution incident on a tungsten foil in simulation.
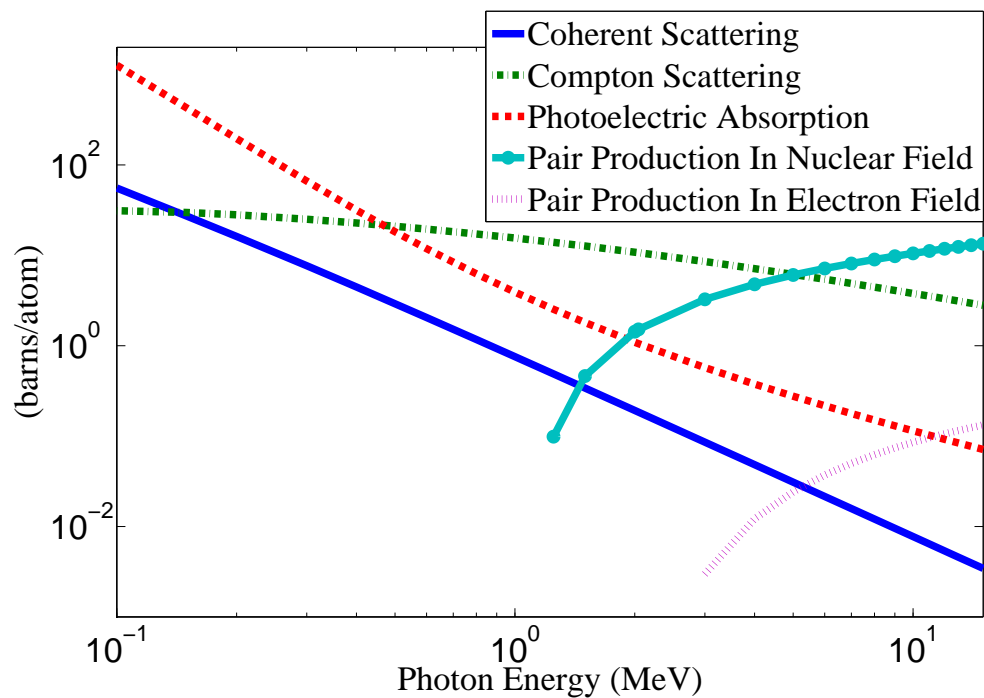
Figure 1.5: Cross section for each type of photon interaction with tungsten as a function of photon energy [9].

Using natural unit, where $c \equiv 1$, the differential cross-section for pair production can be expressed as

$$\frac{d\sigma}{d\epsilon_1 d\theta_1 d\theta_2} = 8 \left(\frac{\pi a}{\sinh(\pi a)}\right)^2 \frac{a^2}{2\pi} \frac{e^2}{\hbar c} \left(\frac{\hbar}{m_e c}\right)^2 \frac{\epsilon_1 \epsilon_2}{k^3} \theta_1 \theta_2$$

$$\times \left\{ \frac{V^2(x)}{q^4} \left[k^2(u^2 + v^2)\xi\eta - 2\epsilon_1\epsilon_2(u^2\xi^2 + v^2\eta^2) + 2(\epsilon_1^2 + \epsilon_2^2)uv\xi\eta cos(\phi)\right] \right. \tag{1.3}$$

$$\left. + a^2 W^2(x)\xi^2\eta^2 \left[k^2(1 - (u^2 + v^2)\xi\eta - 2\epsilon_1\epsilon_2(u^2\xi^2 + v^2\eta^2) - 2(\epsilon_1^2 + \epsilon_2^2)uv\xi\eta \cos(\phi)\right] \right\},$$

where k is photon energy, θ_1 and θ_2 are the scattering angle of e^+ and e^- respectively, $\phi = \phi_1 - \phi_2$ is the angle between the e^+ and e^- pair, ϵ_1 and ϵ_2 are the energy of the positron and electron respectively. Other constants are $u = \epsilon_1\theta_1$, $v = \epsilon_2\theta_2$, $\xi = \frac{1}{1+u^2}$, $\eta = \frac{1}{1+v^2}$, $q^2 = u^2 + v^2 + 2uv\cos(\phi)$, $x = 1 - q^2\xi\eta$, $a = \frac{Ze^2}{\hbar c}$, $V(x) = 1 + \frac{a^2}{(1!)^2} + \frac{a^2(1+a^2)x^2}{(2!)^2} + \frac{a^2(1+a^2)(2^2+a^2)x^4x^2}{(3!)^2} + \cdots$, and $W(x) = \frac{1}{a^2} \frac{dV(x)}{dx}$.

In pair production, positron and electron pairs are created back to back in the center of mass frame. In the lab frame, electrons and positrons tend to move in the direction of the photon, as shown in the Fig. 1.6. The positron and electron carry away the energy from the photon that is in excess of 1.022 MeV. In the center of mass frame, the kinetic energy is equally shared. Photons with an energy above 1.022 MeV in the bremsstrahlung spectrum of the Fig.1.3 have the potential to create electron and positron pairs. The Fig. 1.7 is the simulation of 10 million 12 MeV mono energy electrons impinging on a tungsten target with 1.016 mm thickness. Turning on annihilation process resulted in a 511 keV peak on top of the bremsstrahlung spectrum. This 511 keV peak represents photon produced when the created positrons from the pair production annihilate with atomic electrons inside the tungsten target.
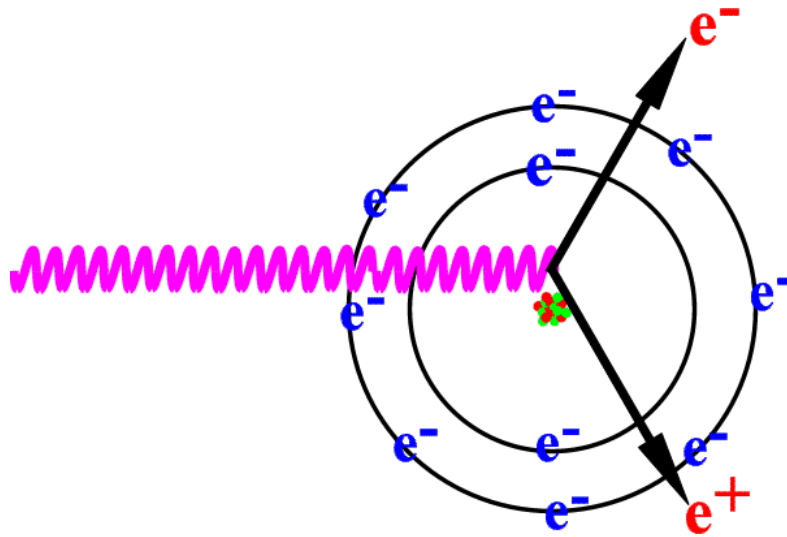
Figure 1.6: Pair production.
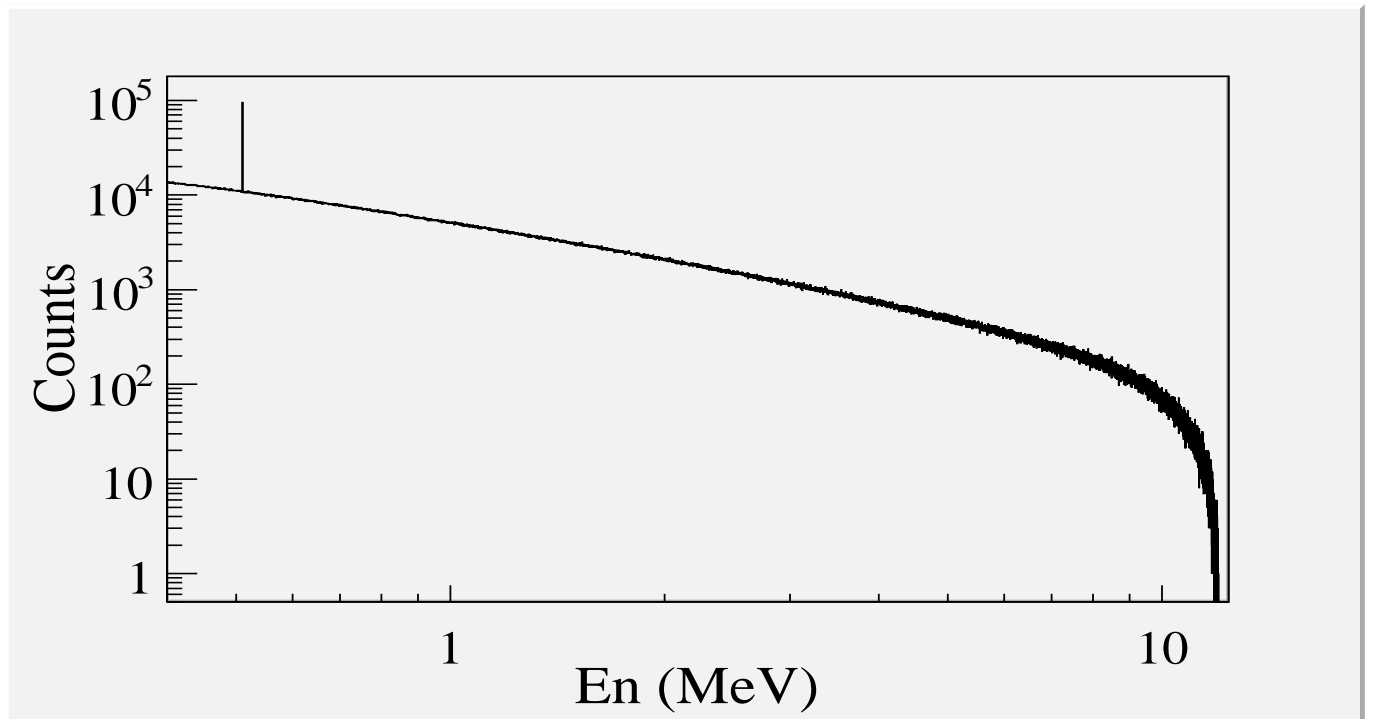
Figure 1.7: Photon spectrum of 10 million 12 MeV mono energy electrons impinging on a 1.016 mm thick tungsten target.

1.3 Emittance Measurement

Emittance is an important parameter in accelerator physics. When the emittance and Twiss parameters are given at the exit of the gun, one will be able to calculate the beam size and the divergence at any given point along the beamline. To study the process of positron creation, one need to know the beam size and divergence on the target. Emittance and Twiss parameters are input parameters for any accelerator simulation tools that can be used to study the experimental processes and to make predictions.

1.3.1 Emittance

In accelerator physics, Cartesian coordinate system is used to describe the motion of the accelerated particles. The z-axis of Cartesian coordinate system is defined as the natural coordinate that is going along the electron beam line. The x-axis and y-axis are horizontal and vertical coordinates which constitute the transverse beam profile. For the convenience of representation, one may use z to represent transverse coordinates and express longitudinal profile with natural coordinates s along the beamline. The transverse beam profiles are described as a function of the longitudinal coordinate, *i.e.* $x(s)$, and $y(s)$. The angle of an accelerated charge regarding the designed orbit can be defined as $z' = \frac{dz}{ds}$.

The phase space z vs. z' of the beam is an ellipse with invariant area (along the beamline). This invariant is called the Courant-Snyder invariant [10]. The transverse emittance ϵ of the beam is defined to be the area of the ellipse, which contains 90% of the particles. Beam divergence and Twiss parameters related to the beam size and divergence is given by

$$\sigma_x(s) = \sqrt{\epsilon_x(s)\beta_x(s)}, \ \sigma_{x'}(s) = \sqrt{\epsilon_x(s)\gamma_x(s)}. \tag{1.4}$$

where ϵ_x is beam horizontal emittance, σ_x is rms beam size, $\sigma_{x'}$ is rms beam divergence, and β_x and γ_x are two of the Twiss parameters.

1.3.2   Emittance Measurement

The HRRL beam emittance was measured using an Optical Transition Radiation (OTR). Transition radiation was theoretically predicted by Ginzburg and Frank [11] in 1946 to occur when a charged particle passes the boundary of two medium and emits radiation. An OTR based viewer was installed to observe electron beam size at the high electron currents, available using the HRRL at 15 MeV with 200 ns macro pulse width and 37.2 mA peak current. The visible light is produced when a relativistic electron beam crosses the boundary of two mediums with different dielectric constants. Visible radiation is emitted at an angle of 90° with respect to the incident beam direction when the electron beam intersects the target at a 45° angle. These backward-emitted photons are observed using a digital camera and can be used to measure the shape and the intensity of the electron beam based on the OTR distribution. Although an emittance measurement can be performed in a several ways [13, 14], the quadrupole scanning method [15] was used to measure the emittance, Twiss parameters, and beam energy in this work.

1.3.3   Quadrupole Scanning Method

Fig. 1.8 illustrates the beamline components used to measure the emittance for the quadrupole scanning method. A quadrupole is positioned at the exit of the linac to focus or de-focus the beam as observed on the OTR view screen. The 3.1 m distance between the quadrupole and the screen was chosen in order to minimize chromatic effects and to satisfy the thin lens approximation. Assuming the thin lens approximation, $\sqrt{k_1}L << 1$, is satisfied, the transfer matrix of a quadrupole magnet may be expressed as

$$\mathbf{Q} = \begin{pmatrix} 1 & 0 \\ -k_1 L & 1 \end{pmatrix} = \begin{pmatrix} 1 & 0 \\ -\frac{1}{f} & 1 \end{pmatrix}, \tag{1.5}$$
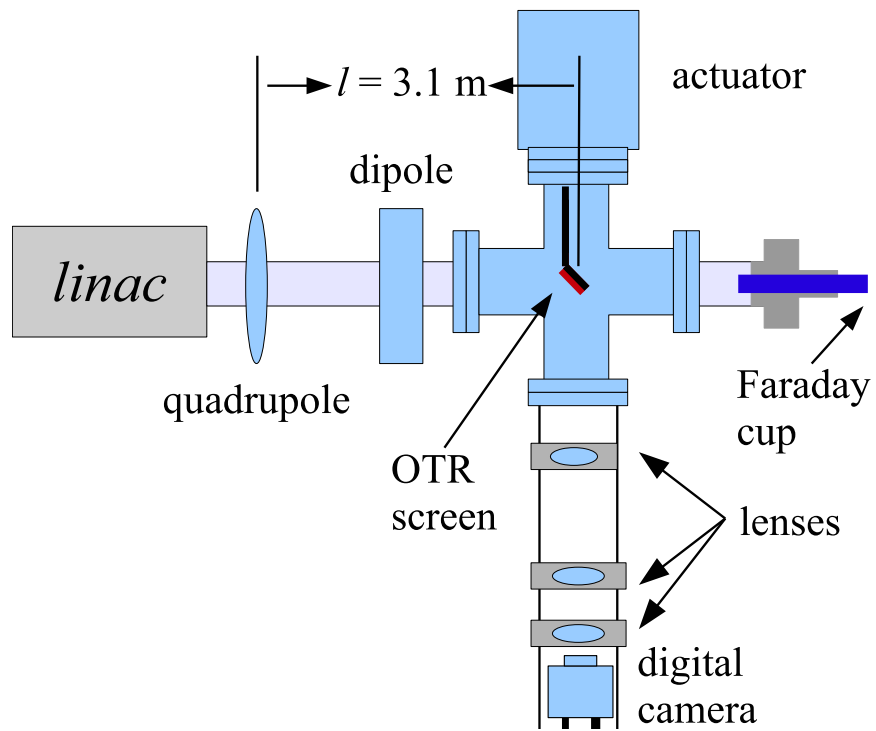
Figure 1.8: Apparatus used to measure the beam emittance.

where k_1 is the quadrupole strength, L is the length of quadrupole, and f is the focal length. A matrix representing the drift space between the quadrupole and screen is given by

$$\mathbf{S} = \begin{pmatrix} 1 & l \\ 0 & 1 \end{pmatrix}, \tag{1.6}$$

where l is the distance between the scanning quadrupole and the screen. The transfer matrix $\mathbf{M}$ of the scanning region is given by the matrix product $\mathbf{SQ}$. In the horizontal plane, the beam matrix at the screen ($\sigma_\mathbf{s}$) is related to the beam matrix of the quadrupole ($\sigma_\mathbf{q}$) using the similarity transformation

$$\sigma_\mathbf{s} = \mathbf{M}\sigma_\mathbf{q}\mathbf{M}^\mathrm{T}. \tag{1.7}$$

where the $\sigma_\mathbf{s}$ and $\sigma_\mathbf{q}$ are defined as [16]

$$\sigma_{\mathbf{s},x} = \begin{pmatrix} \sigma_{\mathrm{s},x}^2 & \sigma_{\mathrm{s},xx'} \\ \sigma_{\mathrm{s},xx'} & \sigma_{\mathrm{s},x'}^2 \end{pmatrix}, \ \sigma_{\mathbf{q},x} = \begin{pmatrix} \sigma_{\mathrm{q},x}^2 & \sigma_{\mathrm{q},xx'} \\ \sigma_{\mathrm{q},xx'} & \sigma_{\mathrm{q},x'}^2 \end{pmatrix}. \tag{1.8}$$

By defining the new parameters [15]

$$A \equiv l^2\sigma_{\mathrm{q},x}^2, \ B \equiv \frac{1}{l} + \frac{\sigma_{\mathrm{q},xx'}}{\sigma_{\mathrm{q},x}^2}, \ \text{and} \ C \equiv l^2\frac{\epsilon_x^2}{\sigma_{\mathrm{q},x}^2}. \tag{1.9}$$

The matrix element $\sigma_{\mathrm{s},x}^2$, the square of the rms beam size at the screen, may be expressed as a parabolic function of the product of k_1 and L

$$\sigma_{\mathrm{s},x}^2 = A(k_1L)^2 - 2AB(k_1L) + (C + AB^2). \tag{1.10}$$

The emittance measurement was performed by changing the quadrupole current, which changes k_1L, and measuring the corresponding beam image on the view screen. The measured two-dimensional beam image was projected along the image's abscissa and ordinate

12

axes. A Gaussian fitting function is used on each projection to determine the rms value, σ_s in Eq. (1.10). Measurements of σ_s for several quadrupole currents $(k_1 L)$ is then fit using the parabolic function in Eq. (1.10) to determine the constants A, B, and C. The emittance (ϵ) and the Twiss parameters (α and β) can be found using Eq. (1.11).

$$\epsilon = \frac{\sqrt{AC}}{l^2}, \quad \beta = \sqrt{\frac{A}{C}}, \quad \alpha = \sqrt{\frac{A}{C}}\left(B + \frac{1}{l}\right). \tag{1.11}$$

== Apparatus ==

Chapter 2

Apparatus

2.1 HRRL Beamline

A 16 MeV S-band High Repetition Rate Linac (HRRL) located at the Beam Lab of the Department of Physics, Idaho State University is used to generate incident 12 MeV electron beam on a tungsten foil. The energy of the HRRL is tunable between 3 to 16 MeV and its repetition rate variable from 1 to 300 Hz. Basic parameters of the HRRL are given in the 2.1. As shown in the Fig. 2.1, the HRRL has a thermionic gun, vertical and horizontal steering magnets sets on two ends and two solenoid magnets.

To construct a beamline that can run on both positron and electron modes, the cavity was relocated to its current position as shown in the Fig. 2.2. The beam elements are described in Tab. 2.2. Quadrupole and dipole magnets were added to the new beamline and diagnostic tools like OTR/YAG screens, Faraday cups and toroids were installed for diagnostic purposes of the electron beam. Energy slits were installed for the control of energy/momentum spread of the beam. A retrievable tungsten foil target (T1) was placed between the 1st and 2nd triplets to produce positrons when the electron beam is incident on it. The room where the

Table 2.1: Basic Parameters of the HRRL.

Parameter	Unit	Value
maximum energy	MeV	16
peak current	mA	100
repetition rate	Hz	300
absolute energy spread	MeV	2-4
macro pulse length	ns	>50
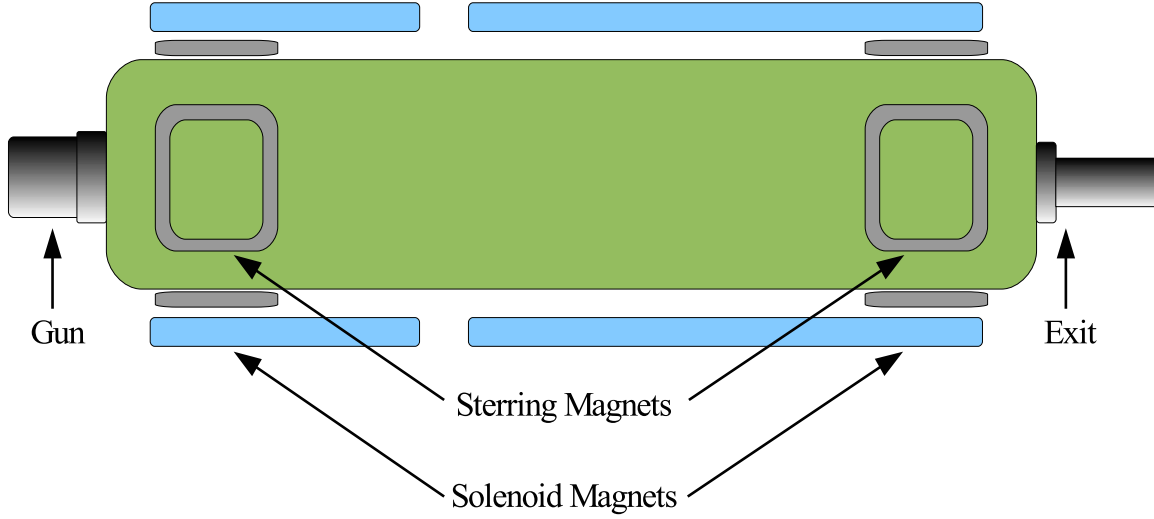
Figure 2.1: The configuration of the HRRL cavity.

HRRL is located is divided by a wall into two parts, the accelerator side and the experimental cell. A beampipe at the end of the 90 degree beamline goes through a hole on the wall and delivers the beam from the accelerator side to the experimental cell. The positron detection system consisting of two NaI detectors is added to the end of the beamline in the experimental cell side as shown in the Fig. 2.2.

2.2 The OTR Imaging System

The OTR target is 10 μm thick aluminum foil with a 1.25 inch diameter. The OTR is emitted in a cone shape with the maximum intensity at an angle of $1/\gamma$ with respect to the reflecting angle of the electron beam [12]. Three lenses with 2 inches of diameter are used for the imaging system to avoid optical distortion at lower electron energies. The focal lengths and position of the lenses are shown in the Fig. 2.3. The camera used is a JAI CV-A10GE digital camera with a 767 by 576 pixel area. The images were taken by triggering the camera synchronously with the electron gun.

16
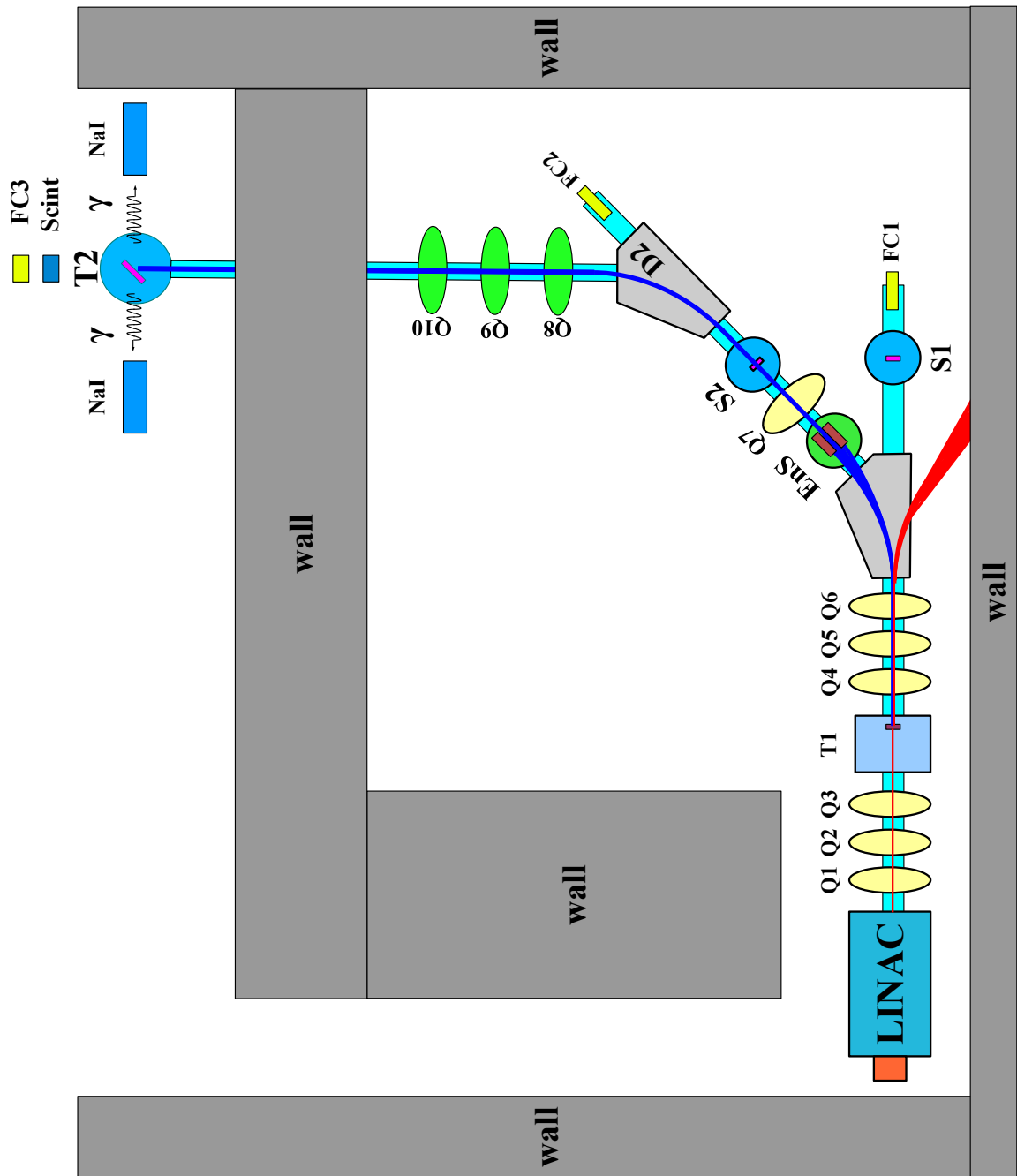
Figure 2.2: The HRRL beamline layout and parts.

Table 2.2: The HRRL Beamline Parts and Their Coordinates.

Label	Beamline Element	Distance from Linac Exit (mm)
Q1	quadrupole	335
Q2	quadrupole	575
Q3	quadrupole	813
T1	e^+ production target	1204
Q4	quadrupole	1763
Q5	quadrupole	2013
Q6	quadrupole	2250
D1	dipole	2680
S1	OTR screen	3570
FC1	Faraday cup	3740
EnS	energy slit	3050
S2	YAG screen	3410
Q7	quadrupole	3275
D2	dipole	3842
FC2	Faraday cup	4142
Q8	quadrupole	4044
Q9	quadrupole	4281
Q10	quadrupole	4571
T2	annihilation target	7381

17 cm

f = 10 cm

18 cm

f = 50 cm

4 cm

f = 5 cm

4 cm
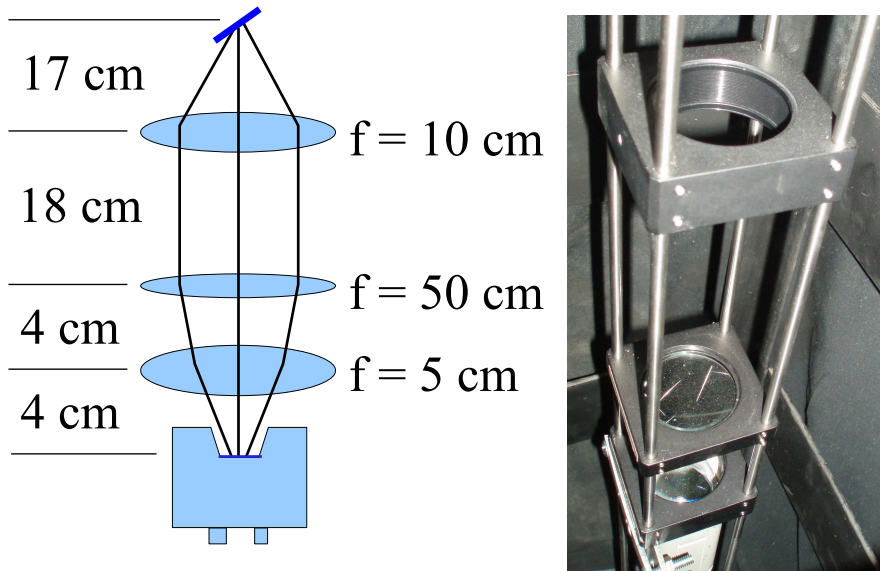
Figure 2.3: The OTR imaging system.
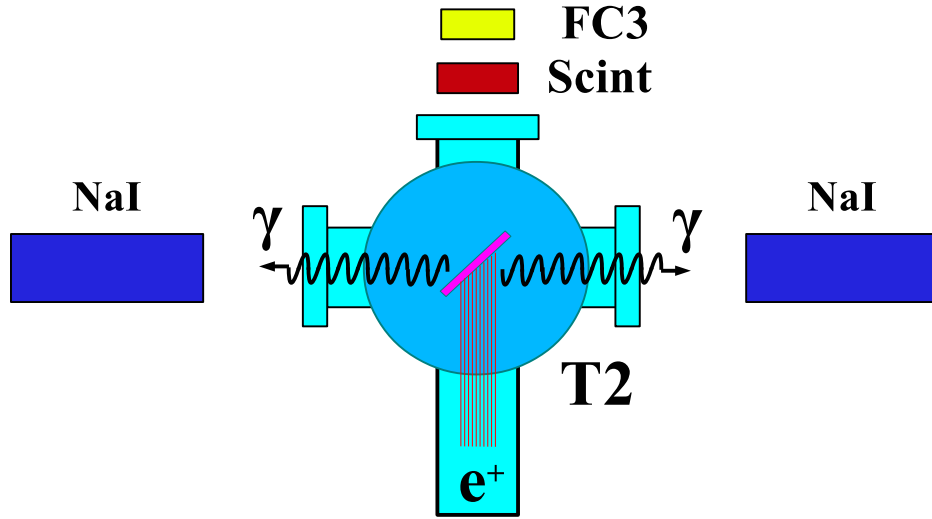
Figure 2.4: Positron Detection System. T2 (pink) is 45 degree placed with horizontal plane, then rotated towards left detector 45 degree.

2.3   Positron Detection

When the electron beam is incident on T1, photon and secondary electrons are created along with positrons. These particles are the main source of noises in the experiment. So, positrons are transported to the second tungsten (T2) which is shielded from noise by the concrete wall and Pb bricks. A 6-way cross is placed at the end of the beamline to hold T2. The 6-way cross has three 1 mil (0.0254 millimeters) thick stainless steel windows. The two horizontal windows perpendicular to the beamline are for the 511 keV photons created during the positron annihilation. The one at the end of the 90 degree beamline is used as the beam exit. Two NaI detectors are placed next to two exit windows to detect the photons produced when positrons are annihilated in T2. The setup is shown in the Fig. 2.4. A scintillator and a Faraday cup are placed at the end of the beamline and are used to tune the electron and positron beam. When positrons reach T2, they are thermalized and annihilated inside T2. During the thermalization, a positron loses its kinetic energy. When it annihilates with an electron, two 511 keV photons are emitted back to back. Two NaI detectors and accelerator RF pulse are in coincidence mode to eliminate noises.

Table 2.3: Radioactive sources and photon peaks.

Radioactive Sources	Unit	First Peak	Second Peak
Co-60	keV	1173	1332
Na-22	keV	511	1275

2.3.1 NaI Detectors

NaI crystals, shown as in the Fig. 2.6, were used to detect 511 keV photons from positron annihilation. Originally, the detectors had pulse lengths around 400 μs. Resistors and capacitors added to the PMT bases and pulse length is shorten to less than 1 μs. The NaI detector has one dynode and one anode outputs. The PMT base configuration of the NaI detector is shown in the Fig. 2.5 and bases made shown in the Fig. 2.7. The crystal is SAINT-GOBAIN CRYSTAL & DETECTORS (MOD. 3M3/3) NaI crystal with sizes of 3" × 3". The PMT base takes HV around -1150 V. It takes ADC 5.7 μs to convert the analog signal to a digital signal. The signal from anode was delayed 6 μs by a long cable and sent to the ADC.

Bases were calibrated using Na-22 and Co-60 sources with photon peaks indicated in the Table 2.3. The Fig. 2.8 is the oscilloscope image of Co-60 photon pulses incident on the detector. The calibrated NaI detector spectrum of Na-22 and Co-60 sources are shown in the Fig. 2.9. The rms values of the fits on the four peaks shown in the Fig. 2.9 are $\sigma_{Na,511} = 18.28 \pm 0.04$ MeV, $\sigma_{Na,1275} = 44.51 \pm 0.27$ MeV, $\sigma_{Co,1173} = 42.49 \pm 0.24$ MeV, and $\sigma_{Co,1332} = 50.30 \pm 0.39$ MeV.

2.3.2 Trigger for The DAQ

The trigger for the DAQ required a coincidence between one or more NaI detectors and the electron accelerator gun pulse. The last dynode signals from left and right NaI detectors were inverted using a ORTEC 474 amplifier and sent to a CAEN Mod. N842 Constant Fraction Discriminator. RF noise from the accelerator was as large as the signal from the NaI detector. Since it was correlated in time with the gun pulse, the gun pulse was used
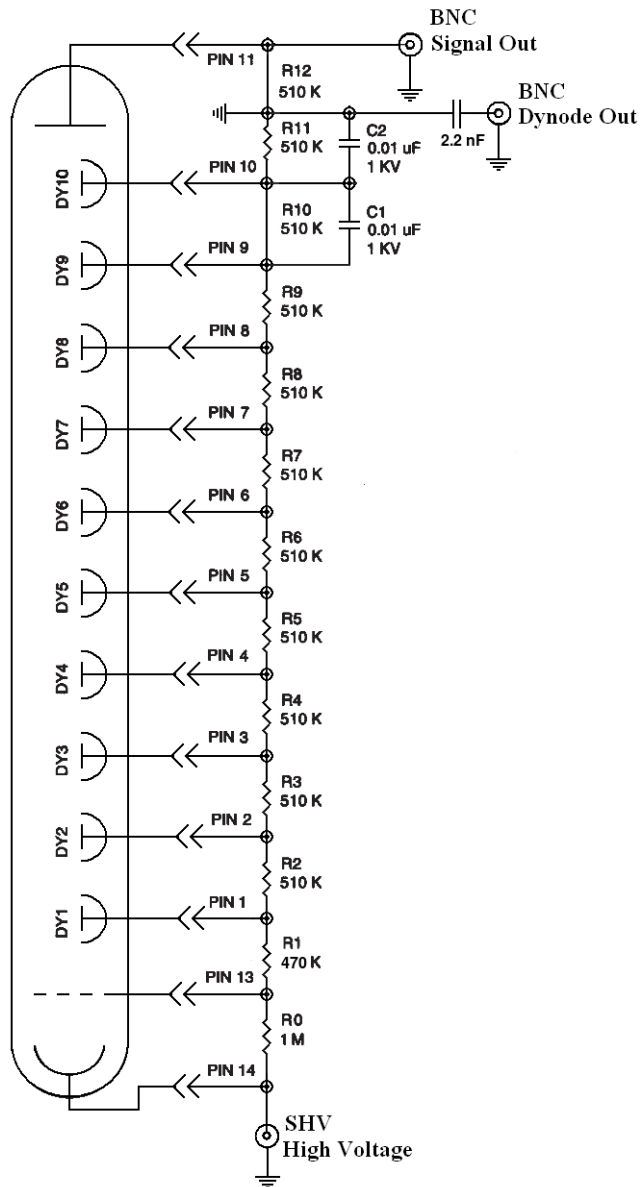
Figure 2.5: Modified PMT base design.
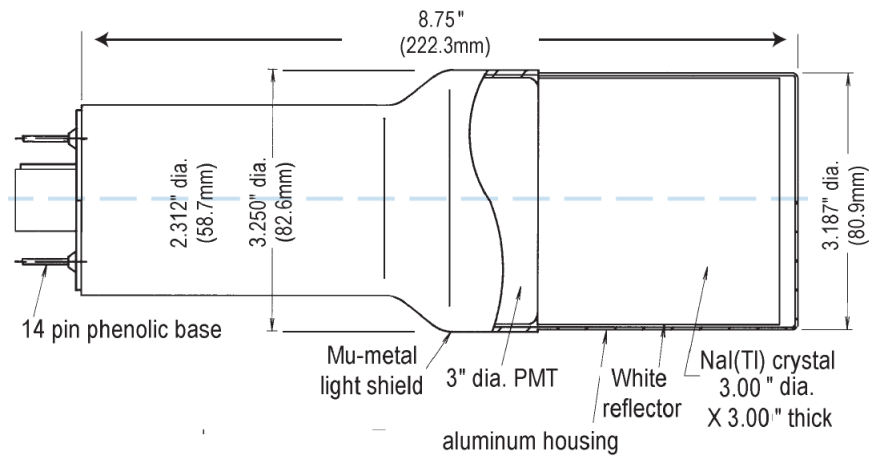
Model 3M3/3

Figure 2.6: NaI crystal dimension.

Figure 2.7: NaI crystals and new bases.
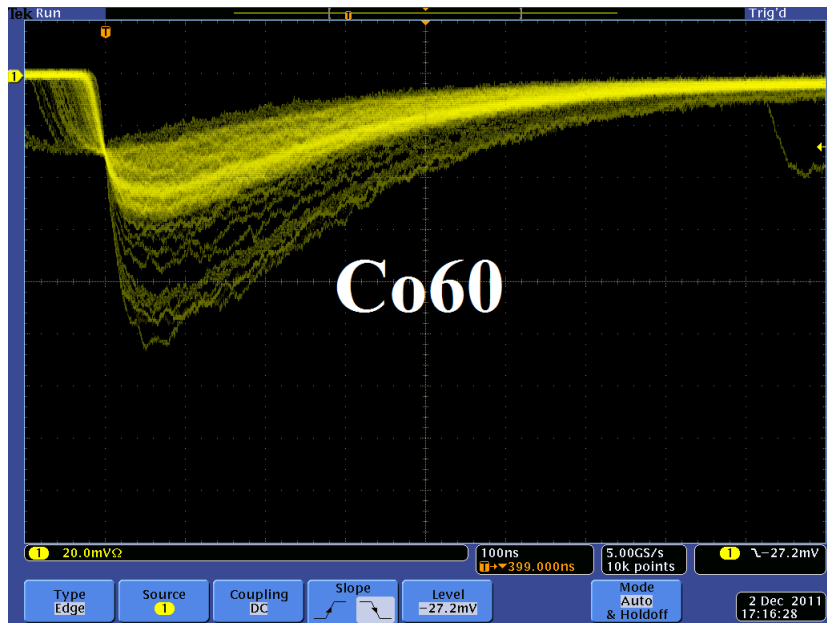
Figure 2.8: Pulses from Co-60 source observed on the scope. The amplitude is about 60 mV. The rise time is larger than 50 ns, and the fall time is larger than 700 ns.
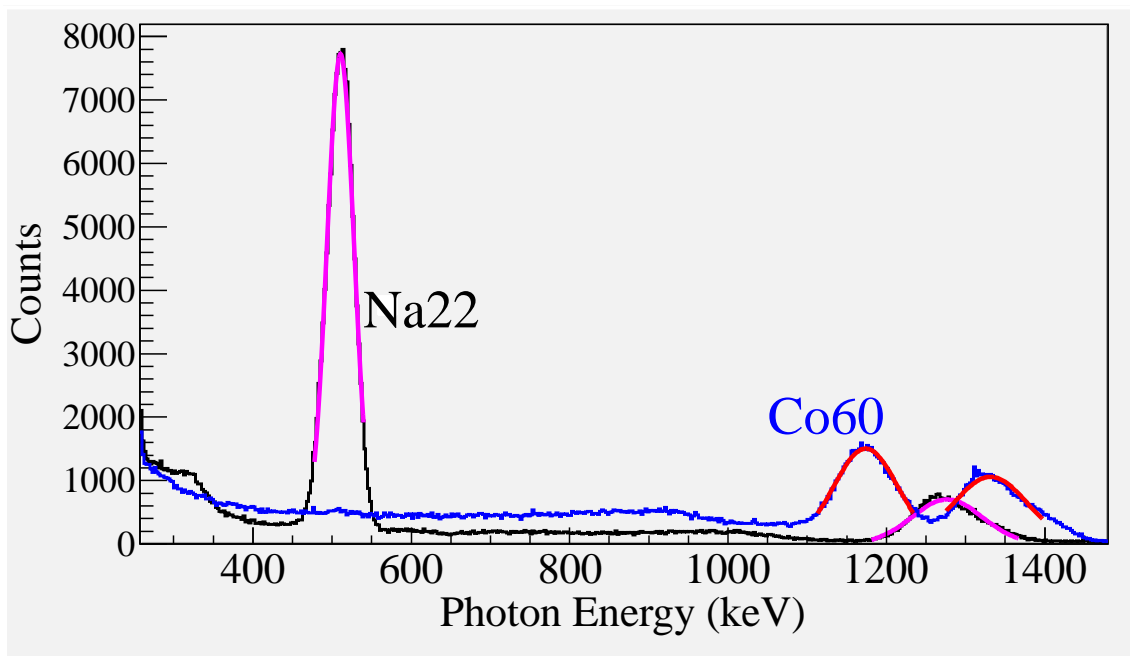
Figure 2.9: Calibrated NaI spectrum of Na-22 and Co-60 sources.

to generate a VETO pulse that prevent the CFD from triggering on this RF noise. After this discrimination and RF noise rejection, the discriminated dynode signals were sent to an GG 8000-01 octalgate generator that increased the width of the logic signals to prevented multiple pulses during a single electron pulse. Then the signals were sent to a LeCroy model 622 quad coincidence to generate AND logic between the electron gun and dynode signals. The logic is set as:

$$(NaI \; Left \; \&\& \; Gun \; Trigger) \; \&\& \; (NaI \; Rgiht \; \&\& \; Gun \; Trigger). \tag{2.1}$$

This is to make sure there is a trigger when photons scatter back to back scatter to the NaI detectors when electron gun is on. Then this trigger was sent to ORTEC Gate & Delay Generator. One of the outputs from the gate generator was used to generate a gate to read analog signal from the anode. Another output was delayed by 6 μs, a necessary time to convert the analog signal from the anode to digital signal, and used as a trigger for the DAQ.

== Simulation ==

Chapter 3

Simulation

A simulation was performed using the package G4beamline [18] to study the processes of position generation and transportation. "G4beamline is a particle tracking and simulation program based on the Geant4 [19] toolkit that is specifically designed to easily simulate beamlines and other systems using single-particle tracking." Since the ratio of e^+/e^- during the positron generation process is very low (on the order of 0.001) and the positron beam loss during the transportation is large, it was necessary to divide the whole process into 3 steps. A new beam event generator is created based on the results of the previous step in the simulation. The first step generates electrons according to a measurement made of the accelerator that was used in the experiment. Electrons were transported to T1 in a vacuum and as a result the interactions of the electron with T1 produced positrons. The second step is the transportation of the positrons generated at T1 to the entrance of the first dipole magnet. The third step is the transportation of the positrons from the entrance of the first dipole magnet to the end of the second dipole, the transportation of the beam from the exit of the second dipole to the T2 target, and the positron beam interaction with T2 and detection of the resulting 511 keV photons.

3.1 Step 1 - The Electron Beam Generation and Tran- spiration to T1

In this step, an electron beam is generated from the experimental measure of electron beam parameters. The Twiss parameters described in the earlier chapter were used to
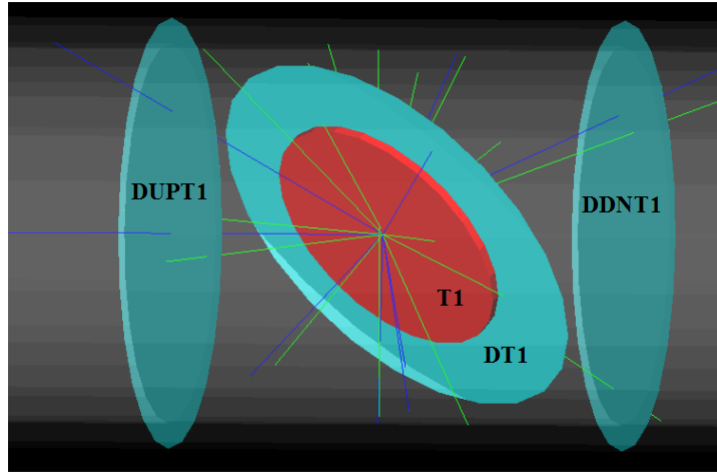
Figure 3.1: T1 is positron production target with same geometry and material as real target. DUPT1 is virtual detector located upstream to sample incoming electron beam. DDNT1 is down stream virtual detector; DT1 is a virtual detector that is placed right after T1 with same angle as T1.

generate electron beam. The energy distribution of the beam is measured and shown in the Fig. 4.4. The blue dots are measurements and the red line are the fit composed of two skewed Gaussian distributions. The fit parameters are given in the Table 4.2 in the previous chapter.

A series of virtual detectors are placed along the beamline to sample the beam. As an example, three detectors and the T1 are shown in the Fig. 3.1. The electron beam is observed at DUPT1 (Detector 25.52 mm UPstream of T1) and positrons (or electrons and photons) generated during the interaction of the electron beam with T1 are observed at DT1 (Detector of T1) and DDNT1 (detector DowN 25.52 mm stream of T1).

3.1.1   Positron Beam on DDNT1

In simulation, 13,799,743,900 electrons are shown by the black line in the Fig. 3.2 incident on T1 created positrons represented by red the line. The blue line is electrons detected downstream of T1. In the Fig. 3.2 1000th of the total number of the particles is shown due
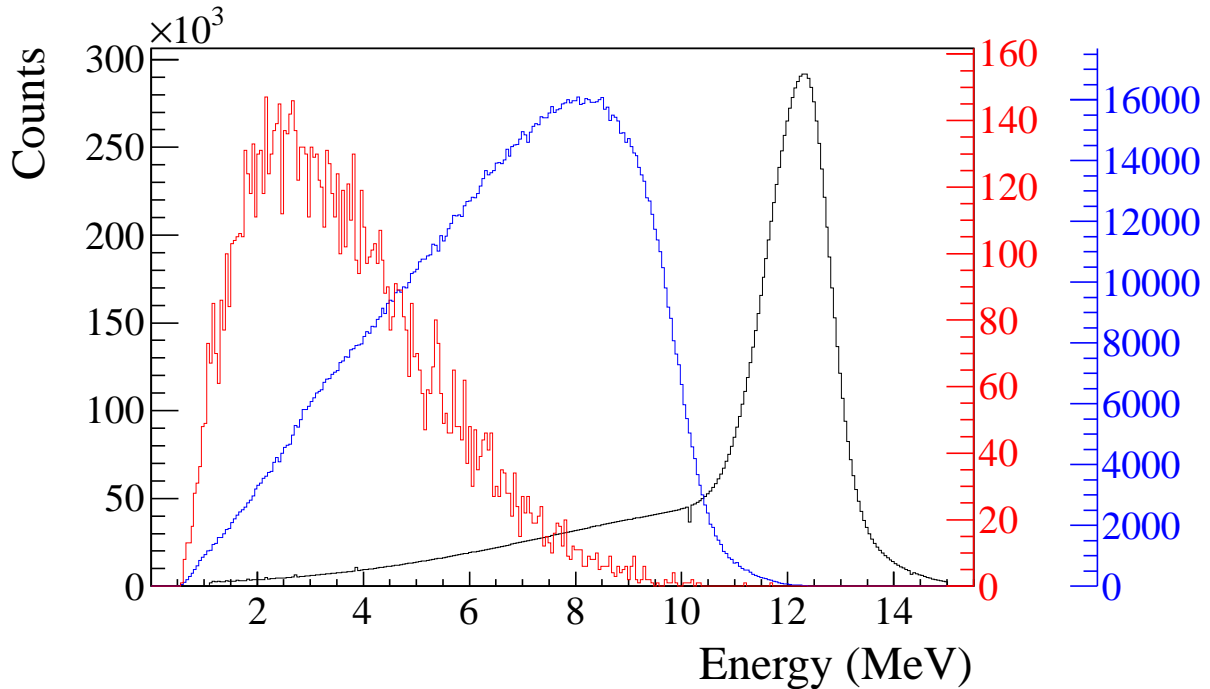
Figure 3.2: Energy distribution of incident electrons (black), electrons after T1 (blue) and created positrons (red).

to the large size. The incident electrons detected by virtual detector DUPT1 and downstream positrons and electrons detected by DDNT1 are shown in the Fig. 3.1.

As can be seen in Figs. 3.3 (b) and (d), the y spatial distribution and divergence of the beam has sharp drops on their left side. The y $vs.$ x distribution of the beam shown in the Fig. 3.3 (e) (sub-figure (f) is zoomed in version of (e)) has a sharp drop in the region between -25.8 mm and -27.2 mm that corresponds to the boundary of the target T1. The Fig. 3.4 shows the geometry of the T1 and the relative location of the virtual detector DDNT1. If the T1 size was increased, it would eventually intersect with the detector DDNT1 at a distance of 25.8 mm from the beam center. A 1.4 mm wide stripe of low counts is visible on DDNT1. This is the result of the target's thickness of 1.016 mm and the 45° angle of intersection ($1.016\sqrt{2} = 1.44$). The edge of the target does not produce many positrons compared to the face of the target.

As shown in Figs. 3.5 (a) and (b), the Y distribution decreases at $\theta = 45°$. Positrons

28
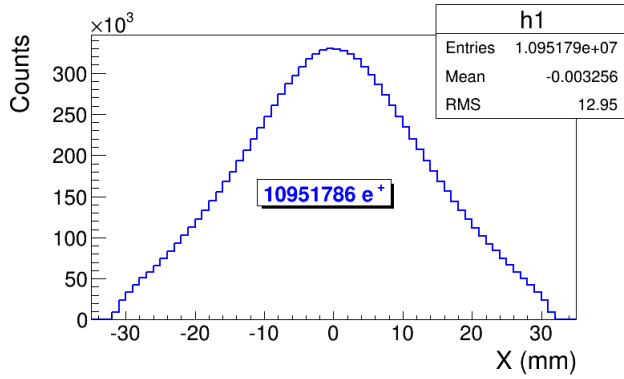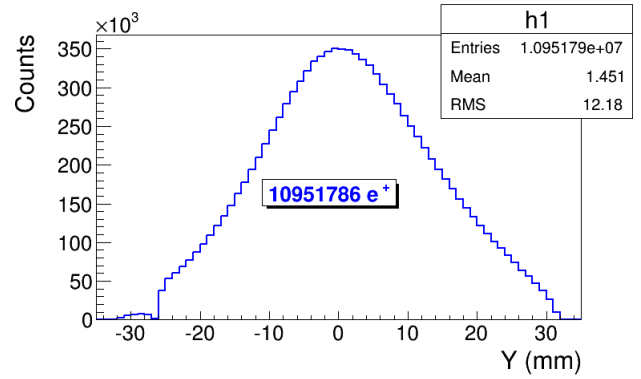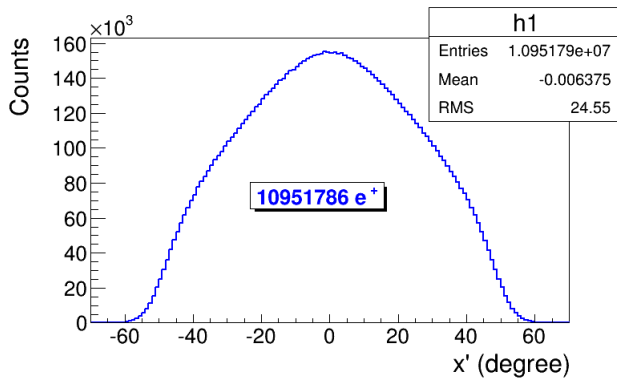
(a) X DDNT1

(b) Y DDNT1

(c) X' DDNT1
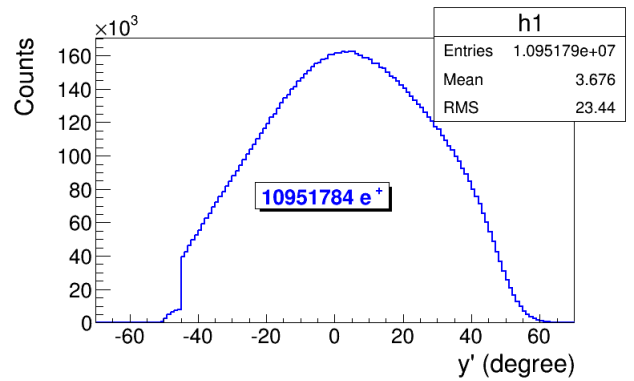
(d) Y' DDNT1
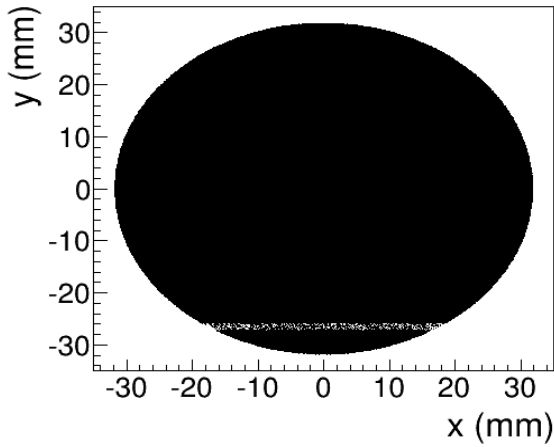
(e) X *vs.* Y DDNT1
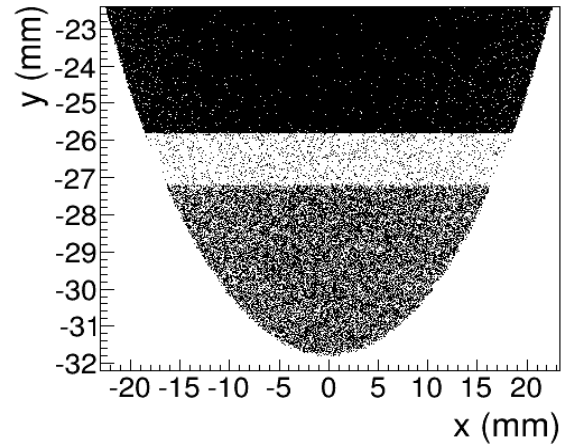
(f) X *vs.* Y DDNT1 zoom

Figure 3.3: Transverse spatial and angular distribution of positrons on the virtual detector DDNT1.
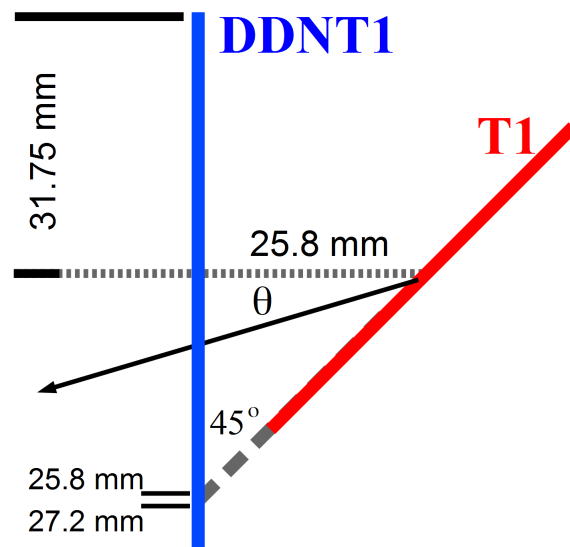
Figure 3.4: Geometry of the target T1 and the virtual detector DDNT1.

(a) Y' *vs*. Y.
(b) Y' *vs*. Y zoom.
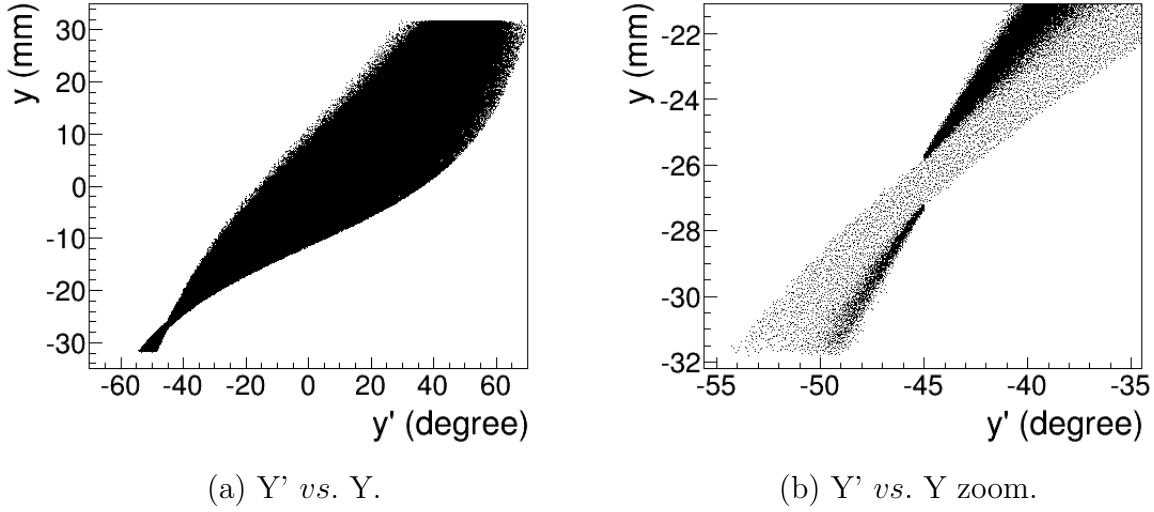
Figure 3.5: Positron beam distribution Y divergence vs. Y spacial distribution on DDNT1.

are emitted from both the downstream and upstream side of the T1. Positrons from the downstream side of the target intersect the detector at angles below 45° while positrons from the upstream side of the target begin to hit the detector at angles beyond 45°. The 1.4 mm gap is the result of the transition of positrons between these two extremes.

3.1.2   Positron Beam on DQ4 and DD1

Resulted positron beam energy distribution on virtual detectors that are placed at the entrance of Q4 (DQ4) and D1 (DD1UP) are shown in the Fig. 3.6. Nearly 90% of positrons are lost when transported from DQ4 to DD1UP due to the large divergence of positrons.

3.2   Step 2 - Transportation of the The Positron Beam after T1 to The Entrance of The First Dipole

In this step, the beam source file is generated by sampling the beam on a virtual detector located downstream of T1 (DDNT1) in previous step. The positrons generated divided into 1 keV/c momentum bins, because higher energy positrons tend to have smaller polar
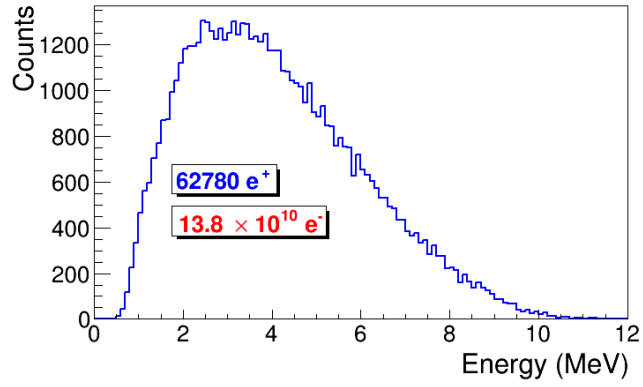
(a) Positron energy distribution on DQ4
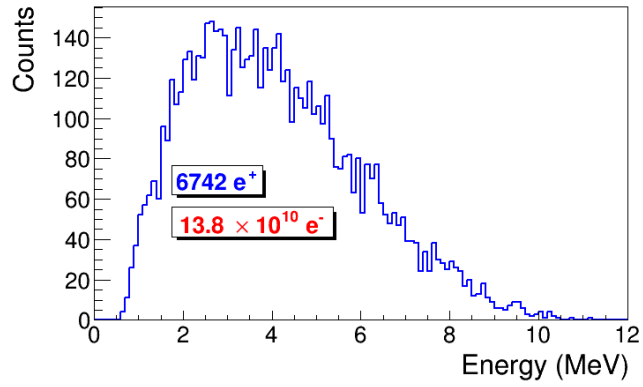
(b) Positron energy distribution on DD1

Figure 3.6: Positron beam energy distribution detected on the downstream of T2.
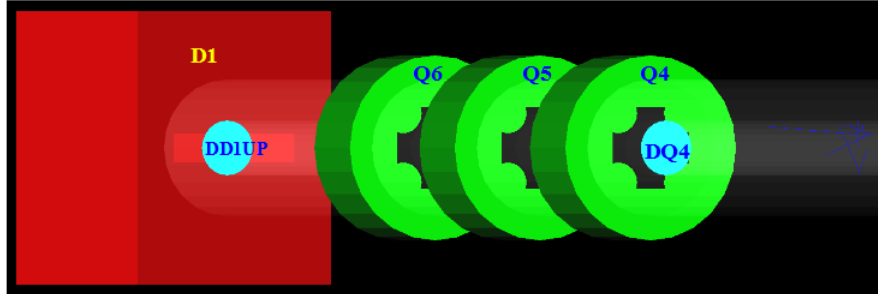
Figure 3.7: Magnets and virtual detectors used in step 2.

angles and vise versa. Because of this correlation, positrons in different momentum bins have different angular distributions. Keeping this correlation in mind, in step 2, each momentum bin is sampled individually. Each momentum bin generates positrons with individual weights, spatial and angular distributions. Positrons generated at downstream of T1 (at detector DDNT1) and transported to the entrance of the D1 are shown in the Fig 3.7. Virtual detectors are placed at the entrance of Q4 (DQ4) and D1 (DD1UP) to track positrons. The beam detected at DD1UP is sampled for the generation of positrons for the next step.
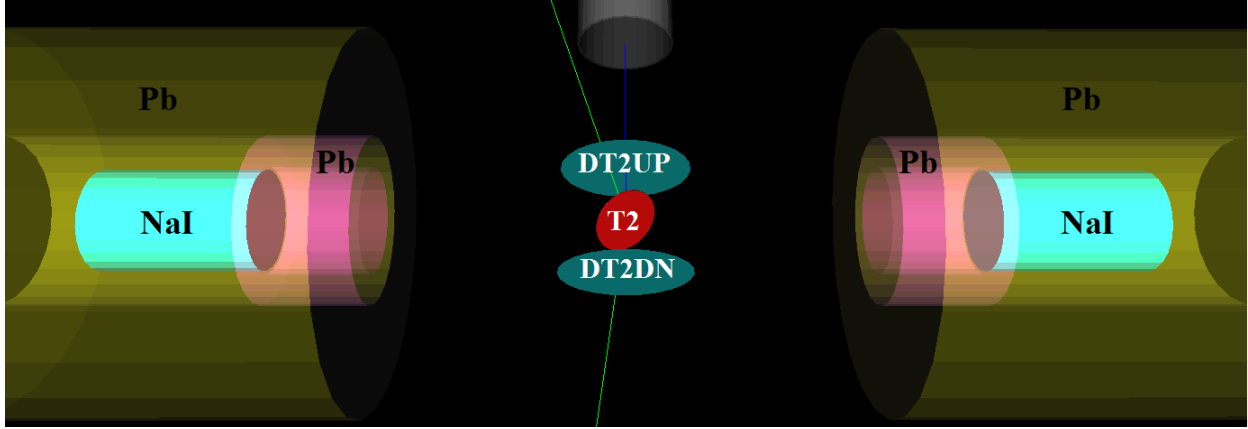
Figure 3.8: T2 and virtual detectors located upstream (DT2UP) and downstream (DT2DN) of T2 are shown at the center of the figure. NaI detectors and Pb shielding are located horizontally at two sides.

3.3 Step 3 - Generation of Positrons at the Entrance of the First Dipole and Their Transporting and Detection

In this step, positrons are generated at the entrance of the first dipole (on DD1UP shown in the Fig. 3.7). The beam source file is generated by sampling the beam on DD1UP in the previous step. The beam then is transported down to T2 located at the end of the beamline as shown in the Fig. 3.8. Two virtual detectors with 48 mm diameter (48 mm is inner diameter of the beam pipe) are placed upstream and downstream of T2 to detect positrons. Two virtual detectors with the same diameter as T2 are placed in parallel to the two sides of T2. NaI virtual detectors are placed horizontally at two sides and 170 mm away from the beamline center to detect photons. 2 inches thick Pb shielding bricks are placed around NaI detectors with 2 inch circular openings facing T2. When a positron annihilates inside T2, two back-to-back scattered 511 keV photons are generated with the same event number. NaI detectors register 1 event when they both detect 511 keV photons with same event number which indicates one positron is being annihilated inside T2.
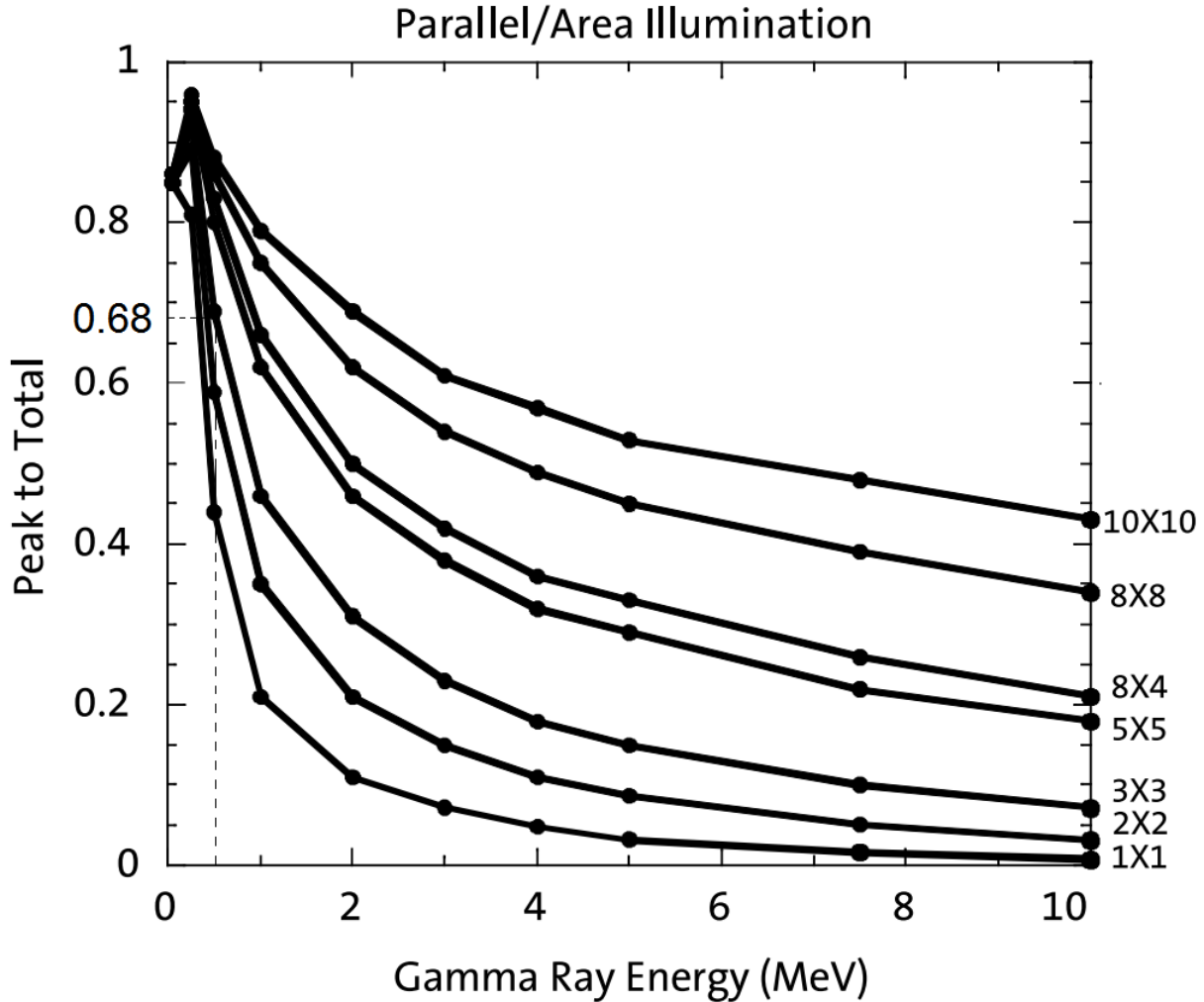
Figure 3.9: NaI detector efficiency obtained from SAINT-GOBIAN CRYSTALS [21].

3.3.1 Positrons Detected by The Detection System.

The detector efficiency chart shown in the Fig. 3.9, obtained from SAINT-GOBIAN CRYSTALS [21], indicates at 511 keV NaI crystals has 68% efficiency. If two detectors are operated in coincidence mode, the detection efficiency of the system should be the multiplication of the individual two detectors, *i.e.* $68\% \times 68\% = 46.24\%$. The Fig. 3.10 shows the counts of 511 keV photons detected (after multiplied to 46.24% efficiency) overlaid with the positrons that are detected on DDNT1.
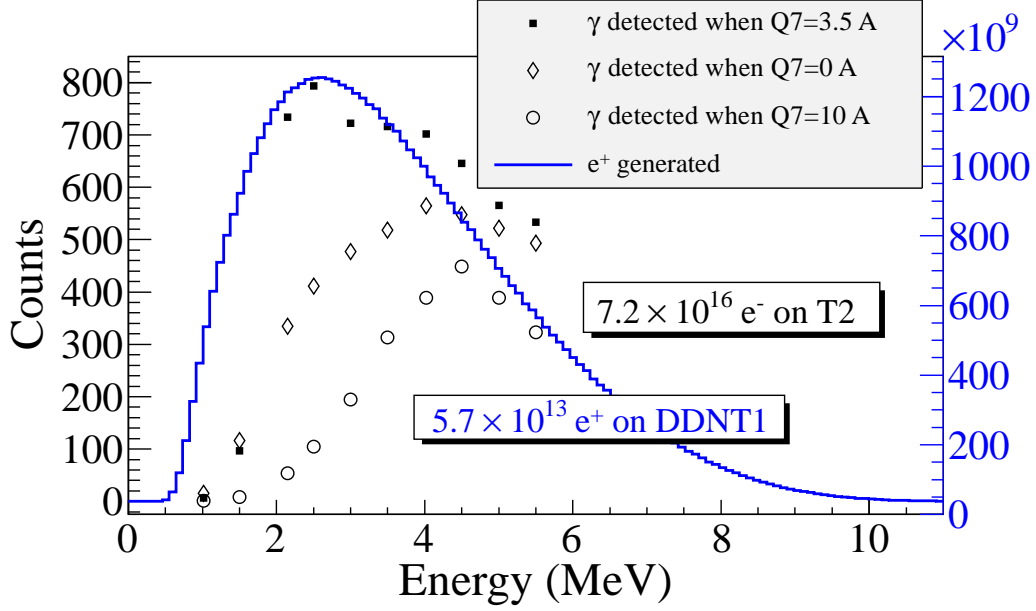
Figure 3.10: Positrons detected on virtual detector DDNT1 and 511 keV photons detected by NaI detectors in coincidence mode when Q7 is at 0 A, 3.5 A and 10 A.

3.3.2 Beam Loss Study

5.756×10^{13} positrons are generated by 7.253×10^{16} electrons incident on T1. Positrons detected along the beamline as shown in the Table 3.1 and the Fig. 3.11 to study the beam losses. 511 keV photons detected by the NaI detector with coincidence mode is shown in the last coulomb of the Table 3.1.

As it can be seen from the Table 3.1, the positrons are divided into 10 bins by energy. At detector DDNT1 (25.8 mm after T1), there are 10^{12} order positrons in each bin. At the entrance of Q4, the counts drop two orders of magnitude. This can be explained by the solid angle that the entrance of Q4 makes. The distance between T2 and the virtual detector DQ4 (which is at the entrance of Q4) is $d = 560$ mm and the radius of DQ4 is $r = 24$ mm (which is inner diameter of beampipe). The solid angle of DQ4 is $\Omega_{q4} = \frac{\pi r^2}{d^2} = \frac{\pi 24^2}{560^2}$. Positrons make up a cone with a 45° half angle which is $\Omega_{beam} = 0.6\pi$ in solid angle. The ratio of the two solid angles, $\Omega_{q4}/\Omega_{beam}$, is 1:160, *i.e.* 1 out of 160 positrons should make it from DDNT1 to DQ4, given that the positrons beam is isotropic inside the cone. However, the positron

Table 3.1: Predicted Number of Positrons Transported and Number of 511 keV Photons Detected.

Energy (MeV)	On DDNT1	Enter Q4	Enter D1	Exit D1	Enter Q7	Enter D2	Exit D2	Reach T2	NaI
1.02 ± 0.25	2.5×10^{12}	1.4×10^{10}	1.4×10^{9}	1.2×10^{8}	2.6×10^{7}	2.7×10^{6}	1.2×10^{6}	4.3×10^{3}	7
1.50 ± 0.25	4.9×10^{12}	2.8×10^{10}	2.8×10^{9}	1.8×10^{8}	9.1×10^{7}	2.7×10^{7}	1.2×10^{7}	5.1×10^{4}	97
2.15 ± 0.25	6.5×10^{12}	3.8×10^{10}	3.8×10^{9}	3.8×10^{8}	1.7×10^{8}	7.8×10^{7}	3.6×10^{7}	4.4×10^{5}	734
2.50 ± 0.25	6.8×10^{12}	4.1×10^{10}	4.1×10^{9}	4.4×10^{8}	2.3×10^{8}	1.1×10^{8}	5.0×10^{7}	4.6×10^{5}	794
3.00 ± 0.25	6.6×10^{12}	4.1×10^{10}	4.1×10^{9}	4.6×10^{8}	2.7×10^{8}	1.3×10^{8}	6.1×10^{7}	4.5×10^{5}	723
3.50 ± 0.25	6.1×10^{12}	3.9×10^{10}	3.9×10^{9}	4.4×10^{8}	2.8×10^{8}	1.4×10^{8}	6.7×10^{7}	4.4×10^{5}	716
4.02 ± 0.25	5.3×10^{12}	3.5×10^{10}	3.5×10^{9}	4.1×10^{8}	2.7×10^{8}	1.4×10^{8}	6.9×10^{7}	4.3×10^{5}	702
4.50 ± 0.25	4.6×10^{12}	3.1×10^{10}	3.1×10^{9}	3.6×10^{8}	2.5×10^{8}	1.3×10^{8}	6.7×10^{7}	4.0×10^{5}	646
5.00 ± 0.25	3.8×10^{12}	2.7×10^{10}	2.7×10^{9}	3.1×10^{8}	2.2×10^{8}	1.2×10^{8}	6.2×10^{7}	3.6×10^{5}	566
5.50 ± 0.25	3.0×10^{12}	2.2×10^{10}	2.2×10^{9}	2.6×10^{8}	1.9×10^{8}	1.0×10^{8}	5.6×10^{7}	3.3×10^{5}	533
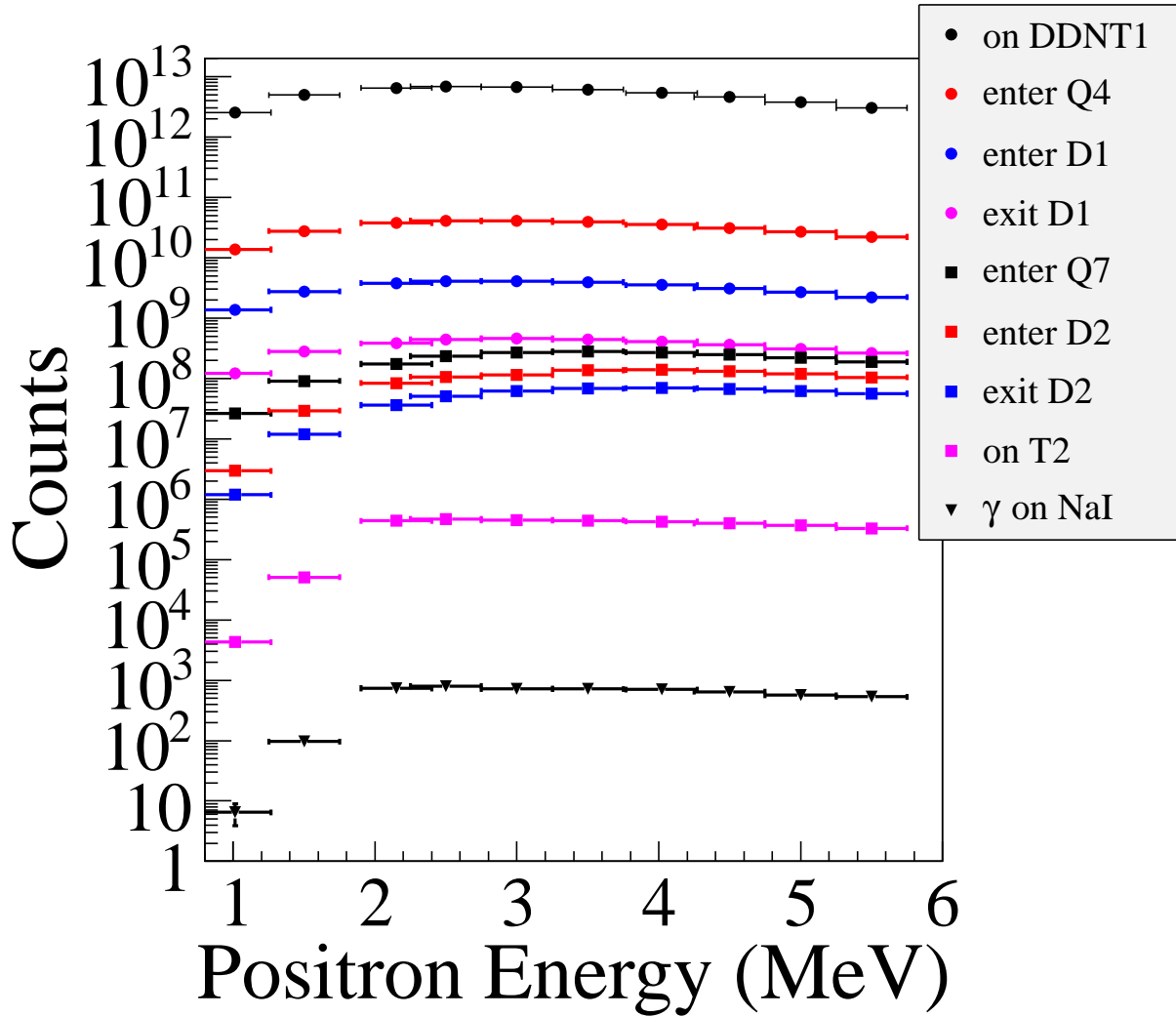
Figure 3.11: Predicted number of positrons transported. Black circle: positrons on DDNT1. Red circle: positrons enter Q4. Blue circle: positrons enter D1. Magenta circle: positrons exit D1. Black cube: positrons enter Q7. Red cube: positrons enter D2. Blue cube: positrons exit D2. Magenta cube: positrons on DT2UP. Black triangle: 511 keV photons detected by NaI detectors in coincidence mode.

beam peaks at a smaller angle as shown in the Fig. 3.3 (c) and (d).

In the Fig. 3.12, dipoles are set to transport 1.436×10^9 (1/10 of the number on the Tab. 3.1) 3 MeV positrons at the entrance of D1. Beam energy distribution is plotted at the exit of D1, entrance of Q7, exit of Q7, entrance of D2, exit of D2, and at T2. 4.1×10^8 positrons enter and 4.6×10^7 exit D1, 2.7×10^7 enter and 2.5×10^7 exit Q7, 1.3×10^7 enter and 6.1×10^6 exit D2. At the end, 4.5×10^5 positrons reach T2. These positrons produced 256195 511 keV photons inside T2 and 255861 escaped T2.

The distance between NaI detectors and the beamline center is 170 cm. The Pb shielding has a hole facing T2 with 2 inches diameter. Assuming positrons annihilated at the center of T2, the solid angle a NaI detector make is $\Omega = \frac{\pi r^2}{d^2} = \frac{\pi 25.4^2}{170^2}$. The 511 keV photons created during the annihilation make a solid angle of 2π considering each side of T2 is facing one detector. The ratio of solid angle of T2 to 2π is about 1:90.

In a simulation with similar settings, as in Table 3.1, dipoles are set to bend 3 MeV positrons. As a result, 4.40041×10^5 3 MeV positrons incident on T2 and created 254864 511 keV photon pairs (*i.e.* 58% of positrons annihilated). A 0.0254 mm thick stainless steel vacuum windows are placed 9 cm from T2 at two sides of the beamline. Two detectors with 24 mm diameter are placed at the two sides of the vacuum window to observe its affect on the photons (1 μm from the window). 4330 511 keV photons went into the vacuum window and 4300 made it through. 0.7% of photon pairs are lost when passing through the vacuum windows.

1518 511 keV photon pairs are detected by NaI detectors in coincidence mode. The ratio 511 keV photon pairs created to the ones detected is 168:1. The left NaI detector detected 2897 511 keV photons and the right one detected 4100. The ratio of 511 keV photon pairs created to ones that made it to the right and the left NaI are 62:1 and 88:1 respectively. Counting photons in coincidence mode cut the rate by half.
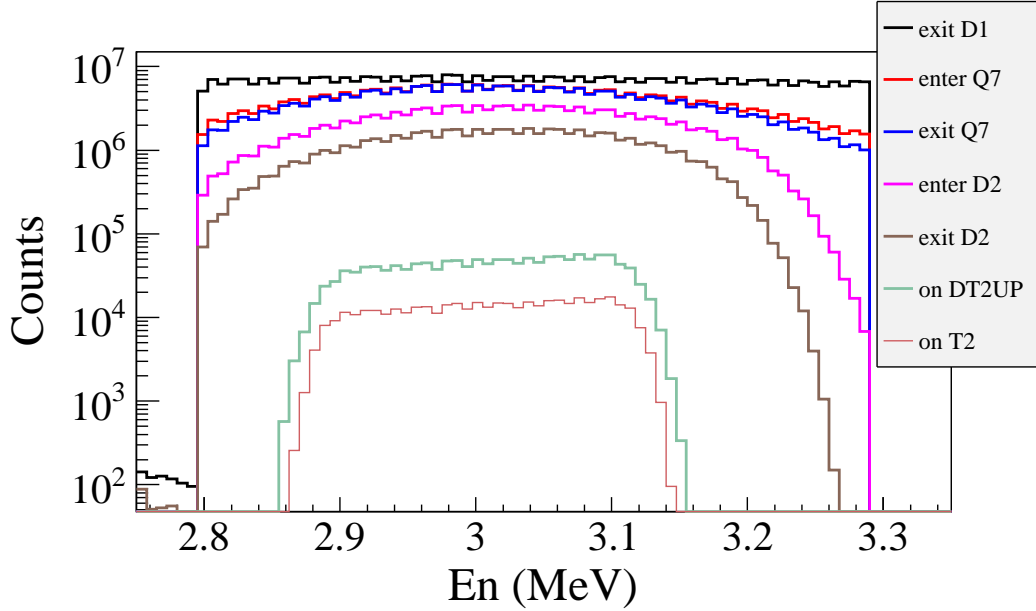
Figure 3.12: Beam transported when dipoles are set for 3 MeV positrons.

3.4 Quadrupole Triplet Collection Efficiency Study

5,475,869,400 positrons generated at DDNT1 and transported to DD1 to study quadrupole triplet positron collection and transportation efficiency. Several quadrupole current settings were simulated as shown in the Table 3.2. As shown in the table, for different quadrupole settings, no significant difference was observed in the number of positrons and their transverse beam profile and momentum distributions. On average, 3590413 positrons detected by DD1. The ratio of positrons generated to the ones that enter D1 is 1525:1.

3.5 Error Study

Systematic error in positron counts is estimated by carrying out simulations with magnet settings as shown Table. 3.3. The NaI detectors have 46.42% efficiency in coincidence mode. The 511 keV photons are counted in coincidence mode, multiplied by 46.42% efficiency and are given in the Table. 3.3. In the table, Max/Min refer to the maximum/minimum magnetic field strength created by the uncertainty in magnet coil current ($\Delta I = 0.1$ A). Def refers to

Table 3.2: Quadrupole Triplet System Collection and Transportation Efficiency Data.

| Q4 | Q5 | Q6 | Entries | x | σ_x | y | σ_y | P_x | σ_{P_x} | P_y | σ_{P_y} | P_z | σ_{P_z} |
A	A	A		mm	mm	mm	mm	MeV	MeV	MeV	MeV	MeV	MeV
-1	2	-1	3587220	-0.005	12	0.030	12	3.0×10^{-5}	0.0461	-0.00216	0.04553	3.848	1.875
-2	4	-2	3591423	-0.012	12	0.049	12	2.2×10^{-5}	0.0461	-0.00211	0.04554	3.848	1.875
1	-2	1	3591509	-0.009	12	0.040	12	-1.5×10^{-5}	0.0462	-0.00216	0.04557	3.849	1.876
1	2	1	3589854	-0.005	12	0.034	12	-1.8×10^{-5}	0.0462	-0.00216	0.04556	3.849	1.876
2	-4	2	3592977	-0.007	12	0.032	12	-3.3×10^{-6}	0.0462	-0.00217	0.04549	3.849	1.876
2	4	2	3589495	-0.004	12	0.033	12	3.0×10^{-6}	0.0462	-0.00218	0.04554	3.849	1.875

the default magnetic field strength. The top 3 rows of the table are the magnet settings and the counts are given in corresponding columns below for the energies given in the left. The fractional error in the 511 keV photon pair counts is calculated by $\frac{|\text{average} - \text{defalt}|}{\text{defalt}}$.

Table 3.3: Systematic Error Study: Counts of NaI Detectors in Coincidence Mode for Different Magnet Settings.

D1	Max	Min	Max	Min	Max	Max	Min	Min	Def		
Q7	Def	Def	Def	Def	Max	Min	Min	Def	Def		
D2	Max	Min	Def	Def	Def	Def	Def	Def	Def		
Energy (MeV)										Average	Fractional Error
0.765 - 1.265	12	2	3	1	1	3	3	0	6	4	57.3 %
1.25 - 1.75	95	75	70	86	85	92	129	86	97	90	17.6 %
1.85 - 2.35	674	724	737	769	686	747	803	681	734	728	5.8 %
2.25 - 2.75	781	755	753	759	772	963	794	763	794	793	8.3 %
2.75 - 3.25	739	737	765	752	738	698	738	757	723	739	2.7 %
3.25 - 3.75	713	699	747	712	707	751	718	705	716	719	2.5 %
3.77 - 4.27	690	708	715	676	704	658	706	715	701	697	2.7 %
4.25 - 4.75	627	666	634	646	635	675	637	653	646	646	2.5 %
4.75 - 5.25	558	595	594	603	606	688	582	582	566	597	6.7 %
5.25 - 5.75	513	536	535	522	525	535	518	544	533	529	1.9 %

== Experiment ==

Chapter 4

Experiment

4.1 Quadrupole Scanning Experiment

Quadrupole scanning method is used to perform emittance measurement. The quadrupole current is changed to alter the strength and direction of the quadrupole magnetic field such that a measurable change in the beam shape is seen by the OTR system. Initially, the beam was steered by the quadrupole indicating that the beam was not entering along the quadrupole's central axis. Several magnetic elements upstream of this quadrupole were adjusted to align the incident electron beam with the quadrupole's central axis. First, the beam current observed by a Faraday cup located at the end of beam line was maximized using upstream steering coils within the linac nearest the gun. Second, the first solenoid nearest the linac gun was used to focus the electron beam on the OTR screen. Steering coils were adjusted to maximize the beam current to the Faraday cup and minimize the deflection of the beam by the solenoid first then by the quadrupole. A second solenoid and the last steering magnet shown in Fig 2.1, both near the exit of the linac, were used in the final step to optimize the beam spot size on the OTR target and maximize the Faraday cup current. A configuration was found that minimized the electron beam deflection when the quadrupole current was altered during the emittance measurements.

The emittance measurement was performed using an electron beam energy of 15 MeV and a 200 ns long, macro pulse of 40 mA current. The current in the first quadrupole after the exit of the linac was changed from -5 A to $+5$ A with an increment of 0.2 A. Seven measurements were taken at each current step in order to determine the average beam width and the variance. Background measurements were taken by turning the linac's electron gun

off while keep the RF on. Background image and beam images before and after background subtraction are shown in the Fig. 4.1. A small dark current is visible in the Fig. 4.1 b that is known to be generated when electrons are pulled off the cavity wall and accelerated.

The electron beam energy was measured using a dipole magnet downstream of the quadrupole used for the emittance measurements. Prior to energizing the dipole, the electron micro-pulse bunch charge passing through the dipole was measured using a Faraday cup located approximately 50 cm downstream of the OTR screen. The dipole current was adjusted until a maximum beam current was observed on another Faraday cup located just after the 45 degree exit port of the dipole. A magnetic field map of the dipole indicates that the electron beam energy was 15 ± 1.6 MeV.

Images from the JAI camera were calibrated using the OTR target frame. An LED was used to illuminate the OTR aluminum frame that has a known inner diameter of 31.75 mm. Image processing software was used to inscribe a circle on the image to measure the circular OTR inner frame in units of pixels. The scaling factor can be obtained by dividing this length with the number of pixels observed. The result is a horizontal scaling factor of 0.04327 ± 0.00016 mm/pixel and vertical scaling factor of 0.04204 ± 0.00018 mm/pixel. Digital images from the JAI camera were extracted in a matrix format in order to take projections on both axes and perform a Gaussian fit. The observed image profiles were not well described by a single Gaussian distribution. The profiles may be described using a Lorentzian distribution, however, the rms of the Lorentzian function is not defined. A super Gaussian distribution was used [17], because rms values may be directly extracted. The Chi-square for x and y profiles are 2.4×10^7 and 1.9×10^7 for super Gaussian fit and 2.6×10^8 and 9.1×10^7 Gaussian fit. The beam spot, beam projections and fits are shown in the Fig. 4.2. In Gaussian distribution, $\phi(x) = \frac{1}{\sqrt{2\pi}} e^{-\frac{1}{2}x^2}$, x on exponent is raised to the 2nd power. In the super Gaussian distribution, x on exponent is smaller than 2, resulting a sharper peak than Gaussian distribution. In Fig. 4.2 the super Gaussian fits raised x on exponent to $N_x = 0.9053$ and $N_y = 1.0427$.

Fig. 4.3 shows the square of the rms (σ_s^2) vs $k_1 L$ for x (horizontal) and y (vertical) beam
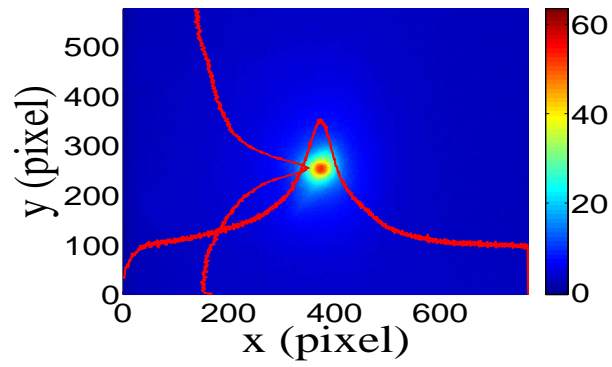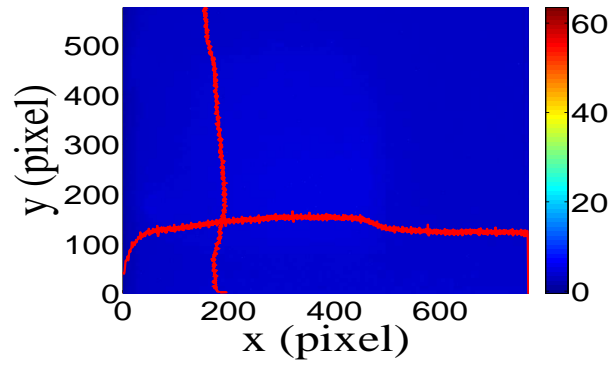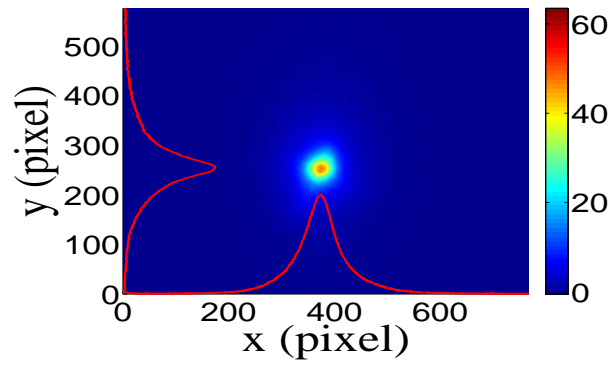
Figure 4.1: Digital image from the OTR screen; (a) a beam with the dark current and background noise, (b) a background image taken when RF is on gun is off, (c) a beam image when dark background was subtracted.
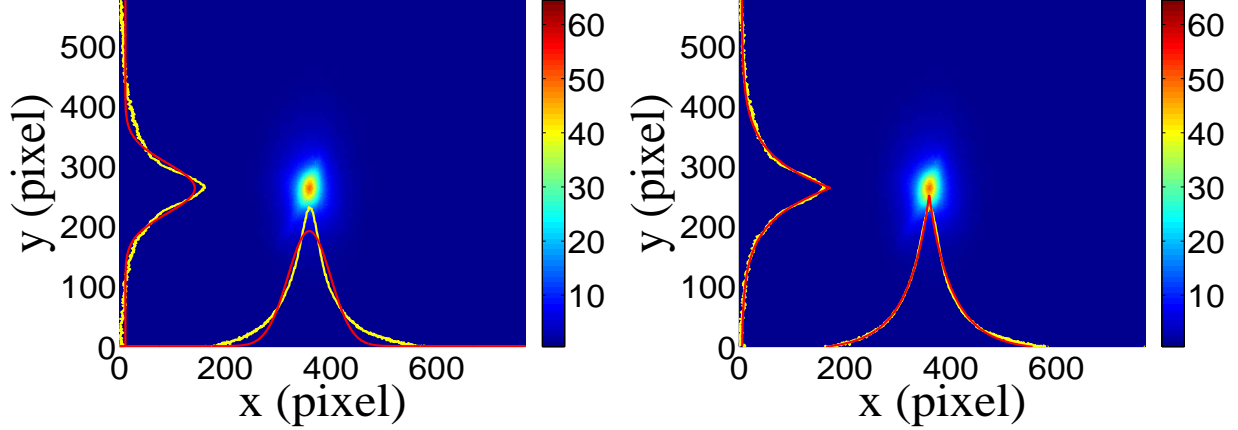
Figure 4.2: Gaussian and super Gaussian fits for beam projections. The beam images is background subtracted image and taken when quadrupole magnets are turned off. Left image is Gaussian fit and right image is super Gaussian fit.

projections along with the parabolic fits using Eq. 4.3. The emittance and Twiss parameters from these fits are summarized in Table 4.1. MATLAB scripts used to calculate emittance and Twiss parameters are given in appendix B.

4.2   Energy Scan

The energy profile of HRRL was measured when it was tuned to accelerate electrons to 12 MeV peak energy. A Faraday cup was placed at the end of the 45 degree beamline to measure the electron beam current when D1 is on and D2 is off. Dipole coil current was changed in 1 A increments and the corresponding Faraday cup current was recorded. The relation between dipole coil current and beam energy is given in the appendix A. As shown in the Fig. 4.4, a 12 MeV peak was observed with a long low energy tail. The energy distribution of HRRL can be described by overlapping two skewed Gaussian fits [17]. The skewed Gaussian fit function is given as,

$$G(En) = A_1 e^{-\frac{-(En-\mu_1)^2}{2(\sigma_1(1+sign(En-\mu_1))E_1)^2}} + A_2 e^{-\frac{-(En-\mu_2)^2}{2(\sigma_2(1+sign(En-\mu_2))E_2)^2}} \qquad (4.1)$$
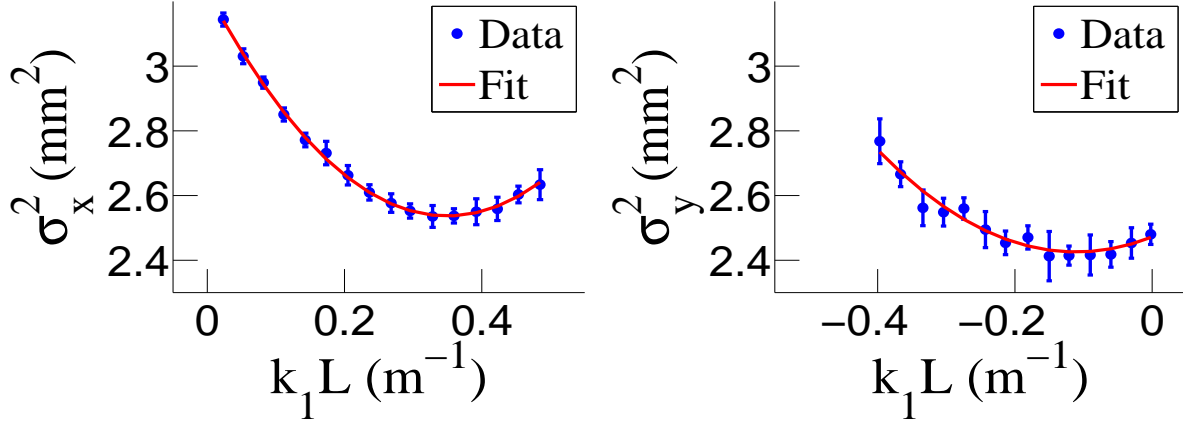
Figure 4.3: Square of rms values and parabolic fittings.

Table 4.1: Emittance Measurement Results

Parameter	Unit	Value
projected emittance ϵ_x	μm	0.37 ± 0.02
projected emittance ϵ_y	μm	0.30 ± 0.04
β_x-function	m	1.40 ± 0.06
β_y-function	m	1.17 ± 0.13
α_x-function	rad	0.97 ± 0.06
α_y-function	rad	0.24 ± 0.07
micro-pulse charge	pC	11
micro-pulse length	ps	35
energy of the beam E	MeV	15 ± 1.6
relative energy spread $\Delta E/E$	%	10.4
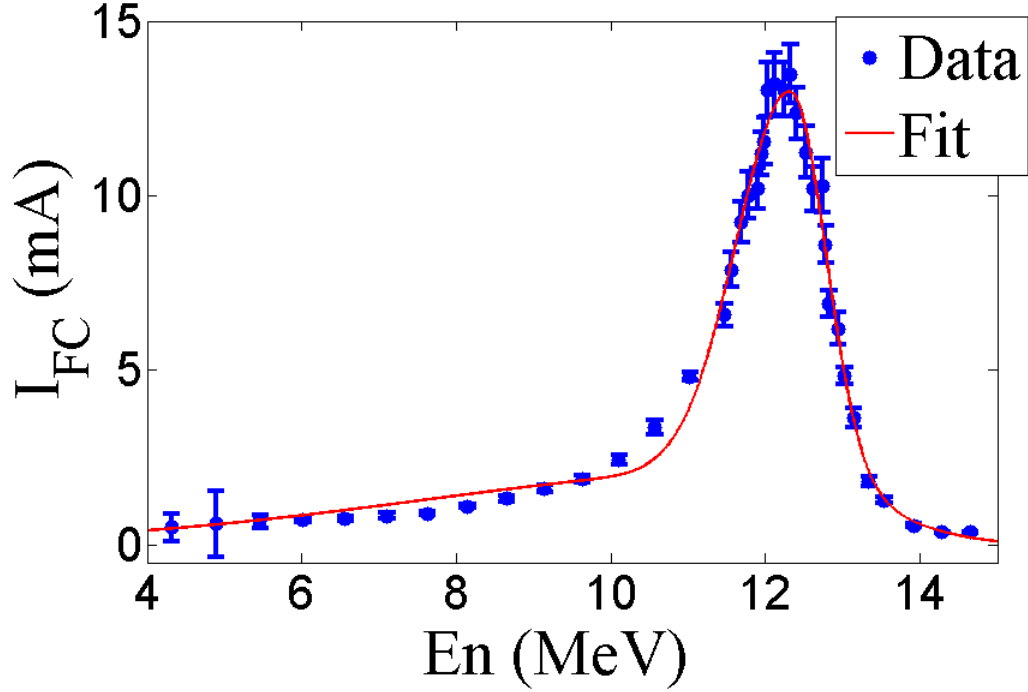
Figure 4.4: HRRL energy scan (blue dots) and fit (red line) with two skewed Gaussian distribution.

where $\sigma_1 = \frac{\sigma_{r,1}+\sigma_{l,1}}{2}$, $\sigma_2 = \frac{\sigma_{r,2}+\sigma_{l,2}}{2}$, $E_1 = \frac{\sigma_{r,1}-\sigma_{l,1}}{\sigma_{r,1}+\sigma_{l,1}}$, and $E_2 = \frac{\sigma_{r,2}-\sigma_{l,2}}{\sigma_{r,2}+\sigma_{l,2}}$. The measurement results and fits are shown in the Fig. 4.4 and in the Table 4.2.

Table 4.2: Two Skewed Gaussian Parameters That Describe Energy Distribution of Electron Beam.

Parameter	Unit	First Gaussian	Second Gaussian
amplitude A	mA	2.14	10.88
mean μ	MeV	12.07	12.32
sigma left σ_L	MeV	4.47	0.70
sigma right σ_R	MeV	1.20	0.45
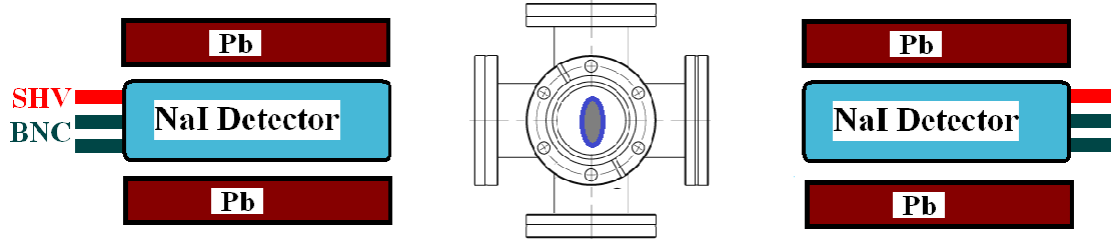
Figure 4.5: Positron detection using T2 and NaI detectors.

4.3 Positron Production Runs

The annihilation target T2 is a tungsten foil that can be inserted or removed from the center of the beamline. This configuration allows two kinds of runs, T2 in and T2 out. When T2 is in, the positions are delivered to T2. Positrons thermalize and annihilate, then produce 511 keV photons. This photons are detected by the NaI detectors as shown in the Fig. 4.5. When T2 is out, positrons exit the beamline and reach the beam dump. NaI detectors are shielded with Pb bricks from the beam dump. T2 out runs are used as background measurements.

T2 is placed inside a 6-way cross with two horizontal sides sealed with thin windows. Two NaI detectors are placed horizontally to T2, perpendicular to the 90 degree beamline with their top pointed to thin windows. The spectrum was taken when the positron beam directed to the end of the 90 degree beamline with T2 in and out are shown in the Fig. 4.6.

Run No. 3735 (T2 in) and run No. 3736 (T2 out) are shown in the Fig. 4.6. The positron counts are extracted by subtracting the background (blue) and integrating the 511 keV peak. On the bottom row in the Fig. 4.6, the red peak is the background subtracted spectrum. The run parameters of run No. 3735 is given in the Table. 4.3.

4.4 Electron Beam Current Measurement

When the electron beam is incident on T1, photons are generated by bremsstrahlung processes. A photon scintillator was placed between Q9 and Q10 as shown in the Fig. 4.7
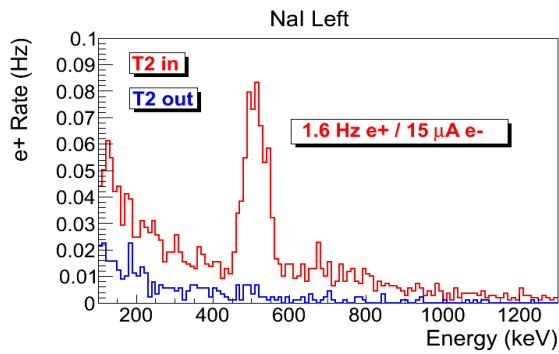
(a) Original spectrum on left NaI.
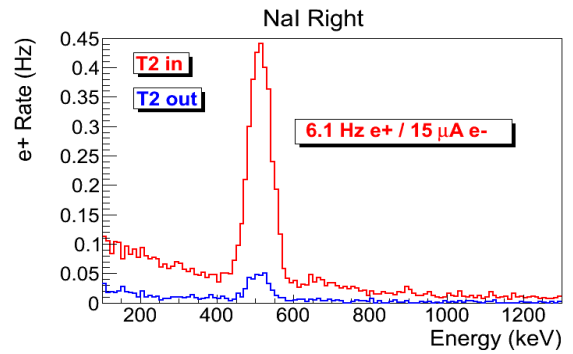
(b) Original spectrum on right NaI.
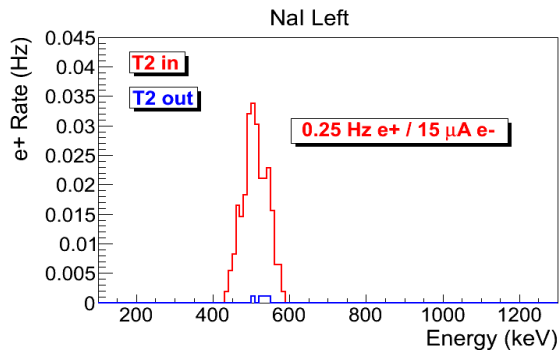
(c) Spectrum with cut on left NaI.
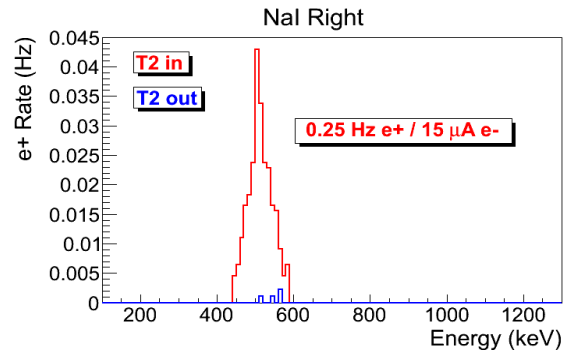
(d) Spectrum with cut on right NaI.

Figure 4.6: Time normalized spectrum of T2 in run (red) and T2 out run (blue). Top row shows original spectrum and bottom row shows incidents happened in 511 keV peak coincidently on both detectors.

Table 4.3: Run Parameters of Run No. 3735.

Parameter	Unit	Value
run number		3735
repetition rate	Hz	300
run time	s	1002
pulses		301462
events		9045
e$^+$ Counts on NaI Detectors		256 ± 16
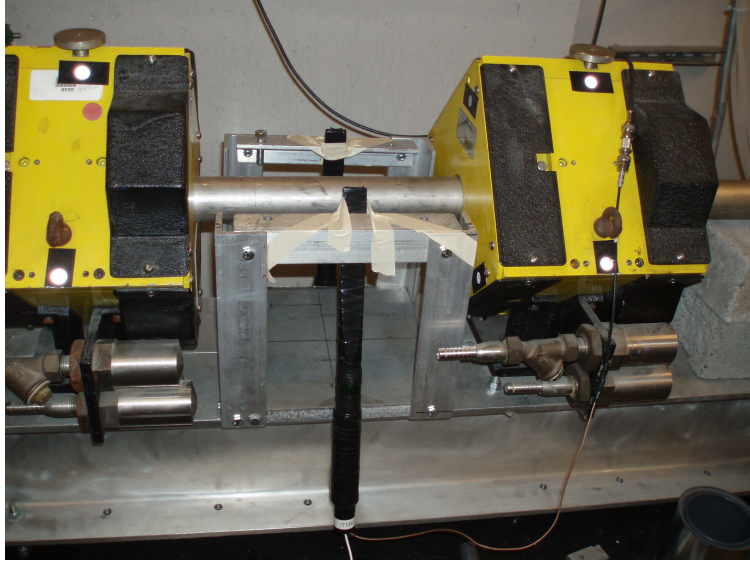
Figure 4.7: Electron beam monitor.

Table 4.4: Scintillator Calibration Data.

Run Number	Faraday Cup Charge Area (nVs)	Mean of ADC Channel 9
3703	1201 ± 10	1126 ± 0.8
3705	777 ± 110	791.8 ± 0.6
3706	367.7 ± 2.3	242.1 ± 0.3

and was used as the electron beam monitor by measuring the photon flux generated by the electron beam. To calibrate the scintillator the electron beam changed incrementally. The electron beam current was measured using the FC1 (Faraday cup 1) and photon flux is measured using the scintillator. The electron current was observed with oscilloscope and photon flux is observed on a Analog to Digital Converter (ADC). As the electron beam decreased, the beam current observed on the oscilloscope decreased and the photon peak in the ADC also shifted towards left end of the photon spectrum as shown in the Fig. 4.8. The measured results are shown in the Table 4.4. The relation between the electron beam current and scintillator ADC channel number is linear and the calibration factor is $(0.93 \pm 0.14)/50$ nVs/(ADC channel number).
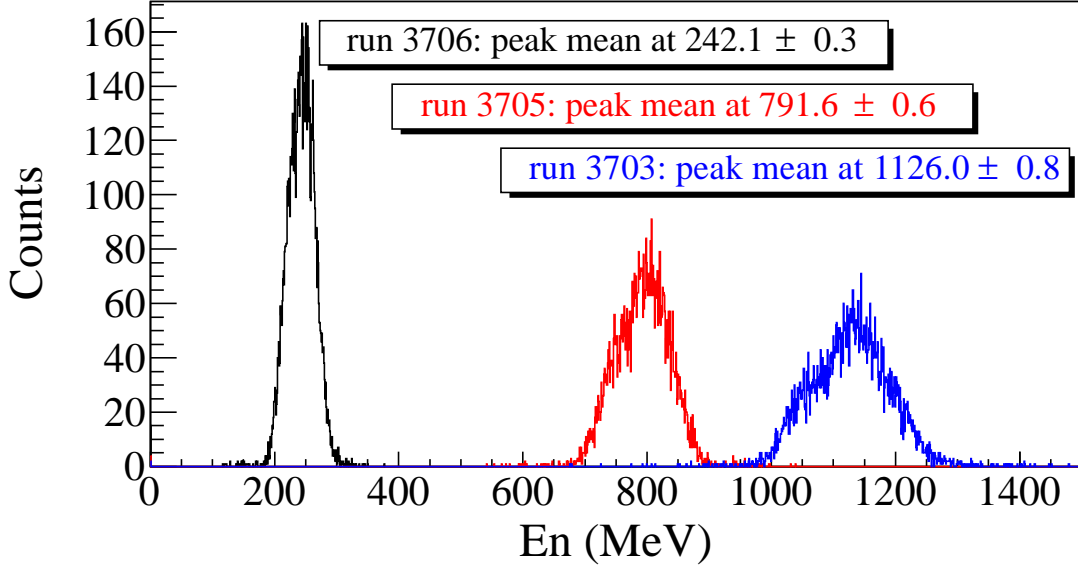
Figure 4.8: The photon flux detected using scintillator and signal sent to the ADC. The mean of the ADC channel decreased linearly as electron beam current decreased.

The average electron beam charge in the experiment calculated with two methods that both uses the ADC. The first method calculates the beam charge detected in each ADC bins and then adds up all the charges as given by

$$Q_{e^-} = \sum_i i \times (bin\ content[i]) \times Q_{Calb} \times (pulses/events). \tag{4.2}$$

In another method, the mean of the of the spectrum multiplied with total number of pulses in the run and calibrated to electron beam charge using calibration factor as given by

$$Q_{e^-} = (Mean\ ADC\ Channel\ Number) \times (pulses) \times Q_{Calb}. \tag{4.3}$$

The average results of the two methods is taken as the final electron beam current. In run 3735, the electron beam charge is $(4.8 \pm 0.5) \times 10^{-3}$ C. The error on electron beam charge is obtained by propagating the error on the calibration factor and finding the variance of the two methods.
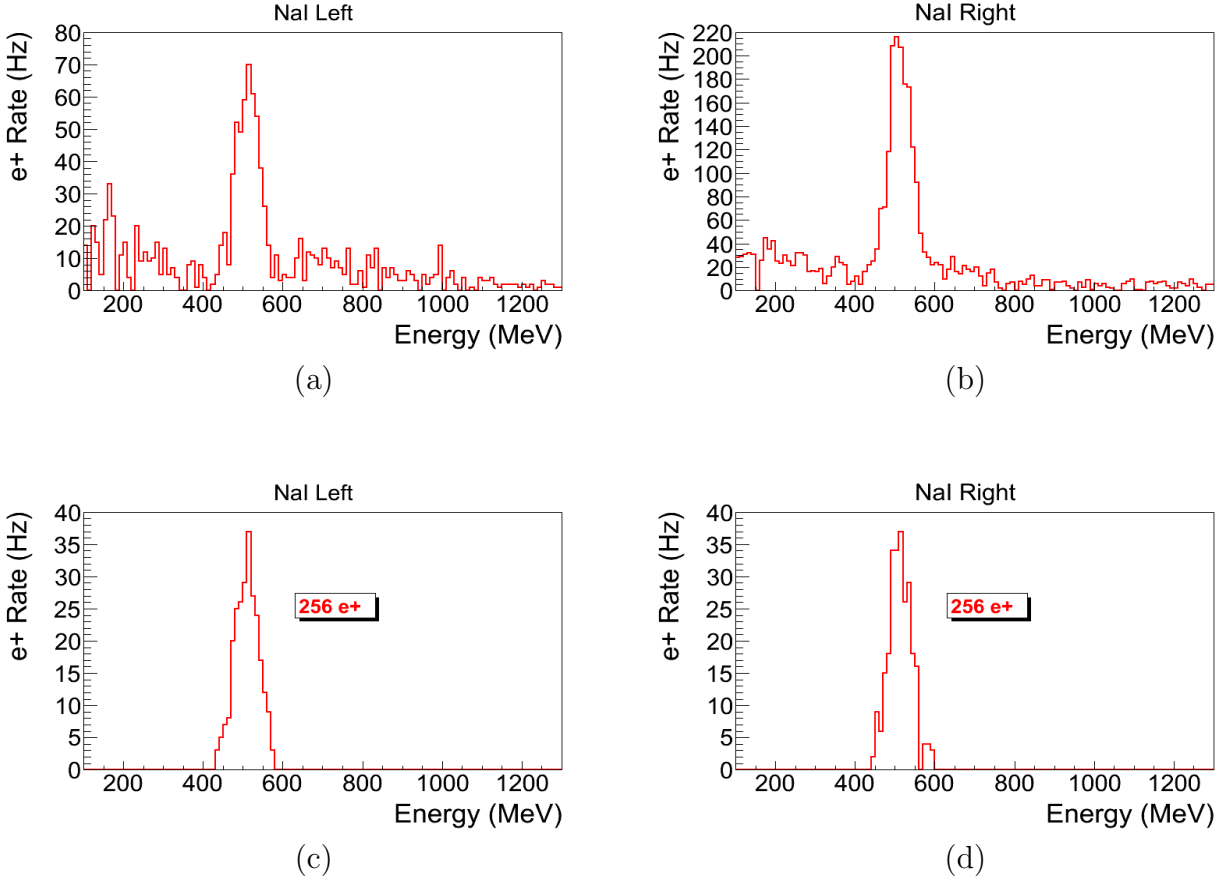
Figure 4.9: Photon spectrum .

4.5   Positron Rate Estimation

The signals from NaI detectors were sent to the ADC. The spectrum shown in the Fig. **??** are the background subtracted spectrum obtained by subtracting counts the counts when T2 is out from the counts when T2 is in. The (a) and (b) are the spectrum of incidents. The (c) and (d) are the spectrum show events that are coincident on both detectors and the photon energy is in the 511 keV peak. The measured ratio of positron to electron is given the Table 4.5 and Fig. 4.10. To find error on the positron beam at different energies, the electron beam is directed to the phosphorous screen at the end of the 90 degree beamline. The positron beam current is too low to be observed on the screen and electron beam was

Table 4.5: Positron to Electron Rate Ratio.

Energy	Positron to Electron Ratio
1.02 ± 0.06	$(0.19 \pm 0.19) \times 10^{-16}$
2.15 ± 0.06	$(0.69 \pm 0.24) \times 10^{-16}$
3.00 ± 0.06	$(8.25 \pm 0.96) \times 10^{-15}$
4.02 ± 0.06	$(4.20 \pm 0.80) \times 10^{-15}$
5.00 ± 0.06	$(0.62 \pm 0.16) \times 10^{-16}$
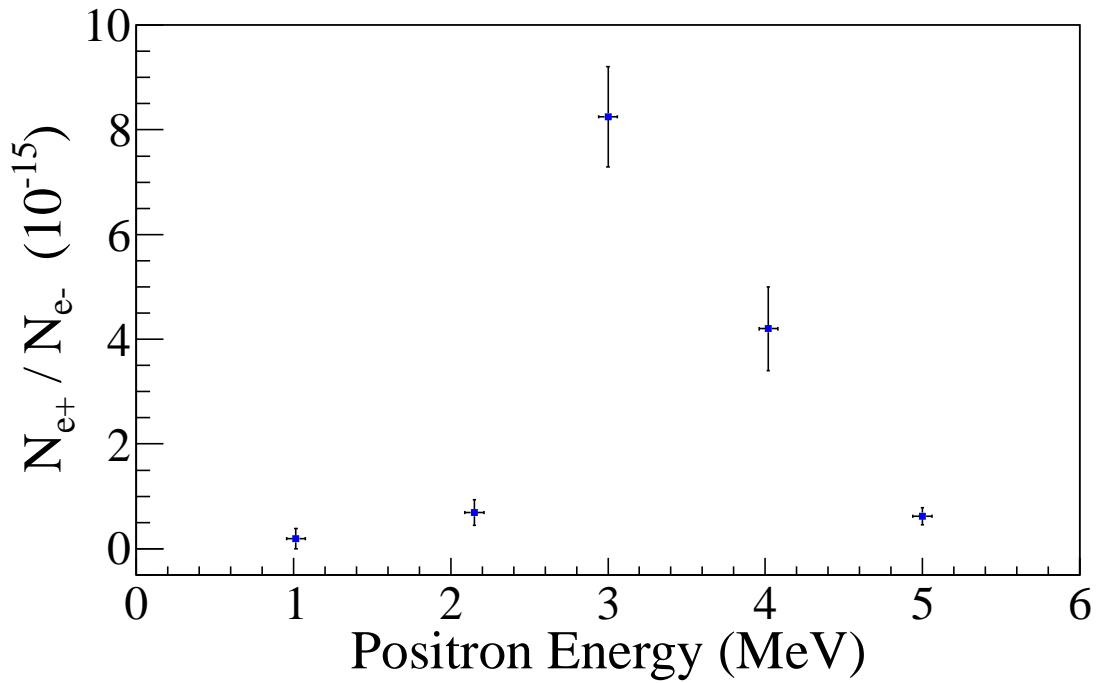
Figure 4.10: Ratio of positrons detected to electrons in experiment.

used to instead. The beam centered and then steered away from the center by changing the current by $\Delta I = 0.1$ A. This 0.1 A change in the dipole current corresponding to 0.06 MeV difference in the beam energy for 3 MeV beam. For other energies, the errors are also 0.06 MeV after rounding up.

The errors on the positron counts are statistical errors. The errors of the positrons to electrons ratios are obtained by propagating the errors of both electron and positron rates.

= Conclusions and Suggestions =

Chapter 5

Conclusions and Suggestions

1. HRRL beamline: The HRRL cavity was placed to new location. New magnetic elements and diagnostic tolls were added to the beamline. The new HRRL beamline was successfully reconfigured to produces positrons while still can transport electrons to the experimental cell.

2. A OTR based diagnostic tool was developed and used to measure the beam emittance of the HRRL. The electron beam profile was not described well using a single Gaussian distribution but rather by a super Gaussian or Lorentzian distribution. The projected emittance of the HRRL was measured to be less than 0.4 μm as measured by the OTR based tool described above when accelerating electrons to an energy of 15 MeV.

3. Successfully constructed the positron detection system using two NaI detectors and the thin tungsten target placed in the 6-way cross.

4. Successfully measured positrons at different energies $(1 - 5 \text{ MeV})$ in experiment. The ratio of positrons being detected on NaI detectors to electrons incident on T2 is on the order of 10^{-15} and the peak observed around 3 MeV.

5. In the experiment quarupoles were optimized to transport 2 MeV due to the limited beam time and it could have diminished transportation efficiency for other energies.

6. Simulation results indicate that the transportation efficiency are varies for different energies. Higher energies has better transportation efficiency. While simulation results agree with experiment in that the peak energy distribution is around 3 MeV, it predicts higher positron to electron ratio as shown in the Fig 5.1.

7. Experimental results show quadrupole magnets are not efficient in collecting positrons, since positrons have large angular distribution. Solenoid might be better option to improve
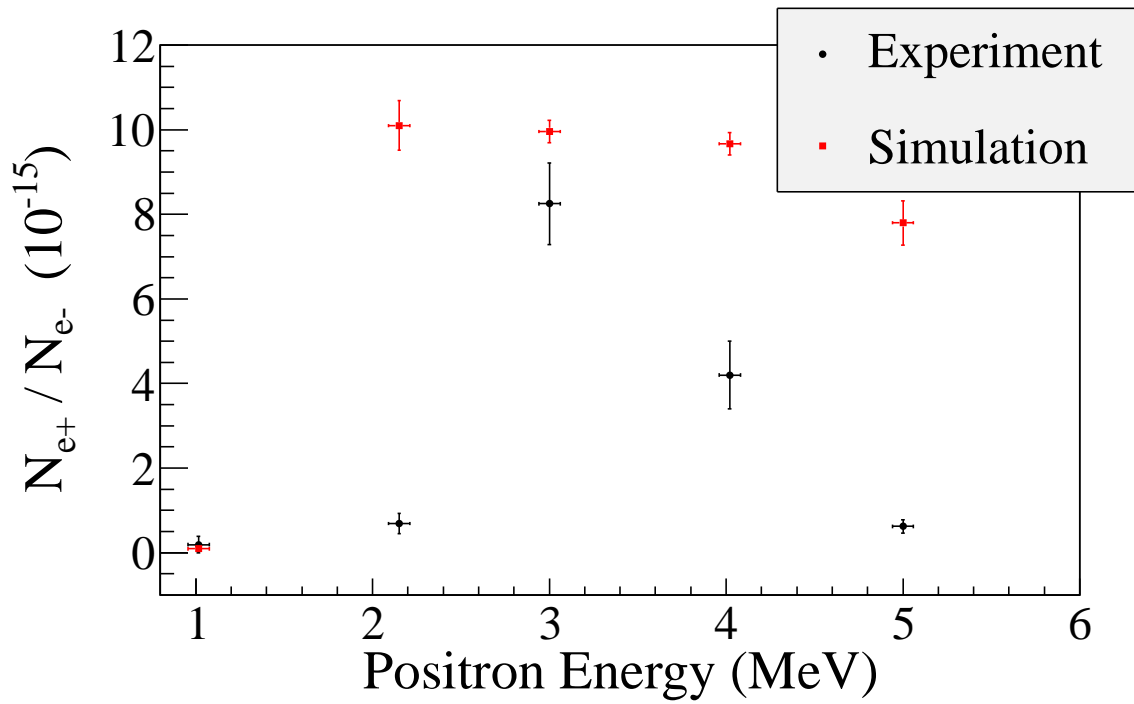
Figure 5.1: Ratio of positrons detected to electrons in experiment and simulation.

the collection efficiency of the positrons. Placing the solenoid close the production target would increase positron transportation efficiency since it can capture more positrons.

Appendix A

Electron Beam Energy Scan

Electron beam energy was scanned using dipole magnet. The dipole magnet was set to bend electron beam with certain energy. The beam current corresponding to that bent electron beam energy was observed on a Faraday cup and oscilloscope.

Table A.1: Dipole Magnet Mapping Data.

Dipole Magnet Coil Current (A)	Faraday Cup Current (mA)	Electron Beam Energy (MeV)
8	0.5	4.3119
9	0.6	4.8896
10	0.67	5.4570
11	0.716	6.0141
12	0.752	6.5610
13	0.828	7.0975
14	0.896	7.6238
15	1.112	8.1399
16	1.328	8.6456
17	1.624	9.1411
18	1.896	9.6262
19	2.448	10.1012
20	3.36	10.5658

Continued on next page

Dipole Magnet Coil Current (A)	Faraday Cup Current (mA)	Electron Beam Energy (MeV)
21	4.82	11.0201
22	6.58	11.4642
22.2	7.88	11.5518
22.5	9.24	11.6824
22.7	10.0	11.7690
23	10.2	11.8980
23.1	11.2	11.9408
23.2	11.56	11.9836
23.3	13.04	12.0262
23.5	13.2	12.1111
23.8	13.04	12.2377
24	13.48	12.3216
24.2	12.36	12.4050
24.5	11.24	12.5295
24.7	10.2	12.6119
25	10.28	12.7348
25.1	8.6	12.7756
25.2	6.92	12.8162
25.5	6.2	12.9376
25.7	4.84	13.0180
26	3.64	13.1378
26.5	1.82	13.3354
27	1.28	13.5305

Table A.1 – *Continued from previous page*

Dipole Magnet Coil Current (A)	Faraday Cup Current (mA)	Electron Beam Energy (MeV)
28	0.56	13.9129
29	0.364	14.2850
30	0.364	14.6469

Appendix B

MATLAB Scripts for Calculating Emittance

The main script

`"Emit_Calc.m`

loads and digitize electron beam images. By projecting the 2D beam to the axis, 1D beam profile is extracted and passed to

`SupGau_devsum.m`

for super Gaussian fitting.

`SupGau_devsum.m`

returns rms of the super Gaussian fit. The rms values of different images are sent to

`Emit_Parabola_Fit_kl_XProjection`

.

`Emit_Parabola_Fit_kl_XProjection`

fits parabola for given rms values, plots the fit and extract emittance from the fit.

B.1 Emittance Calculator

```
% Emit_Calc.m
% Reads images from files and digitize images.
% Fits a super Gaussian funtion on the projection, get the rms values.
% Then pass them to fit parabola
%
% April-2011
% Sadiq Setiniyaz


clc;
clear


me = 0.511; % electron rest mass in MeV
%En = 14; %enter beam energy here in MeV unit.
En = 14.9985 ; %14.9985 MeV energy at Mar 17th, 2011.
En_er = En*0.1; % Assume 5% error on Energy
L = 0.08; % pole face is 8 cm long in z direction.
R_Bore = 0.0254; %Radius of the Bore aperture = center to pole face = 1 inch.
%L_ef = L + R_Bore;
%I_max_neg = -10; %enter smallest negative scan current. Here -7 Amps
%I_max_pos = 7; %enter biggest positive scan current. Here 10 Amps
I_start=-3.0; % Scan starting current
%I_end=-2.0; % Scan ending current
I_increment=0.2;
scan_current_number=31; % do 13 scan.
scan_times=7;
```

```
%for ii = 1:scan_step
%    I(ii) = I_start + (ii-1)*I_increment;
%end


p = sqrt(En*En - me*me)/1000;% e- momentum in GeV/c


%%%%%%%%%%%%%%%%%%%%%%%%%%%%%%%%%%%%%%%%%%
% Enter the distance from the center of the quad to the screen
S12=3.1;%(in m unit) S12(q4)=1.875 cm. S12(q1)=3.10 cm
erS12 = 0.005; % assume 51 mm error.
%%%%%%%%%%%%%%%%%%%%%%%%%%%%%%%%%%%%%%%%%%


%%%%%%%%%%%%%%%%%%%%%%%%%%%%%%%%%%%%%%%%%%%%%%%%%%%%%%%%%%
%Enter calibration here:
calibration_x=0.04327*0.001; %m/px
calibration_y=0.04204*0.001; %m/px
er_calibration_x=0.00016*0.001;
er_calibration_y=0.00018*0.001;
%%%%%%%%%%%%%%%%%%%%%%%%%%%%%%%%%%%%%%%%%%%%%%%%%%%%%%%%%%


disp('Reading image ...')
% Get image for background. For background RF is on, gun is off.


bg1 = imread('Scan_1\RF_on_Gun_off_bg.bmp');
bg2 = imread('Scan_2\RF_on_Gun_off_bg.bmp');
bg3 = imread('Scan_3\RF_on_Gun_off_bg.bmp');
bg4 = imread('Scan_4\RF_on_Gun_off_bg.bmp');
```

```matlab
bg5 = imread('Scan_5\RF_on_Gun_off_bg.bmp');

bg6 = imread('Scan_6\RF_on_Gun_off_bg.bmp');

bg7 = imread('Scan_7\RF_on_Gun_off_bg.bmp');

% Averaging background.

bg = (bg1+bg2+bg3+bg4+bg5+bg6+bg7+bg7+bg7)/7;

imd_bg = double(bg(:,:,1));


for ii=1:scan_times
switch ii
    case 1
        addpath(genpath('\Scan_1'));
    case 2
        addpath(genpath('\Scan_2'));
    case 3
        addpath(genpath('\Scan_3'));
    case 4
        addpath(genpath('\Scan_4'));
    case 5
        addpath(genpath('\Scan_5'));
    case 6
        addpath(genpath('\Scan_6'));
    case 7
        addpath(genpath('\Scan_7'));
end


% Read OTR images.
for scan = 1:scan_current_number;
    thisfilename=ii;
```

```matlab
    imNo = ii;
    I(scan) = I_start + (scan-1)*I_increment;
    switch scan
        case 1
% Devide the effetive length by 100 to convert to meter unit.
            im = imread('negative\11.bmp');
            tifname='11';
            L_ef(scan) = 9.95/100;
            Er_L_ef(scan) = 0.17/100;
        case 2
            im = imread('negative\12.bmp'); % reading 1.png
            tifname='12';
            L_ef(scan) = 9.91/100;
            Er_L_ef(scan) = 0.16/100;
        case 3
            im = imread('negative\13.bmp');
            tifname='13';
            L_ef(scan) = 9.91/100;
            Er_L_ef(scan) = 0.16/100;
        case 4
            im = imread('negative\14.bmp');
            tifname='14';
            L_ef(scan) = 9.85/100;
            Er_L_ef(scan) = 0.14/100;
        case 5
            im = imread('negative\15.bmp');
            tifname='15';
            L_ef(scan) = 9.85/100;
```

```matlab
                Er_L_ef(scan) = 0.16/100;
            case 6
                im = imread('negative\16.bmp');
                tifname='16';
                L_ef(scan) = 9.87/100;
                Er_L_ef(scan) = 0.19/100;
            case 7
                im = imread('negative\17.bmp');
                tifname='17';
                L_ef(scan) = 9.82/100;
                Er_L_ef(scan) = 0.19/100;
            case 8
                im = imread('negative\18.bmp');
                tifname='18';
                L_ef(scan) = 9.86/100;
                Er_L_ef(scan) = 0.17/100;

    end
    sg = im; % reading 1.png
imd_sg = double(sg(:,:,1));
pic = (imd_sg-imd_bg);
%imd = imd_sg;
%imd = imd_bg;

% Noise Cleaning.
% Getting red of the dead pixels.
% If there is sudden increase in the pixel brightness,
% Then use the pixel brightnesss of the earlier pixel.
for i = 3:768
```

```
for j = 3:576
    if pic(j,i)>500
        pic(j,i)=pic(j-1,i);
    elseif pic(j,i)-pic(j-2,i)>20
            pic(j,i)=pic(j-1,i);
    end
end
end

% Determine image size in pixels.
dim=size(pic);
%dim=size(imd);
dim_x = dim(1);
dim_y = dim(2);


xunit='m';
yunit='m';


% Beam transverse profiles.
profx = sum(pic,1); % make x projection
profy = sum(pic,2)';% make y projection


xbins=size(profx);
ybins=size(profy);
x=(1:1:xbins(2));
y=(1:1:ybins(2));


% Set Gaussian fit range.
```

```matlab
xl = 1;
xr = 766;
yl = 1;
yr = 576;


% Checking.
%plot(x,profx,'k');
%hold on;
%plot(y,profy,'k');
%hold on;


% Initialize fit parameters.
% a1= base. a2 = A; amplitude. a3 = mean. a4 = D; sigma_0. a5 = N;
a1 = 100;
a2 = 7700;
a3 = 280;
a4 = 39;
a5 = 1;


% SupGau = a(1)+a(2)*exp(-abs(X-a(3))/(a(4))).^a(5); % super gaussian.
% Putting the parameters together.
a0 = [a1,a2,a3,a4,a5];
% Setting fit criteria and use fminsearch optimization.
opts = optimset('TolX',1e-4,'MaxFunEvals',10000,'MaxIter',10000,'Display','on');
% Pass fit parameters to SupGau_devsum.
[fitpara_x,fval_x,flag_x,err_x] = fminsearch(@SupGau_devsum,a0,opts,x,profx);
[fitpara_y,fval_y,flag_y,err_y] = fminsearch(@SupGau_devsum,a0,opts,y,profy);
% Get the fit parameters of x profile.
```

```
base_x = fitpara_x(1);

amplitude_x = fitpara_x(2);

peak_center_x = fitpara_x(3);

sig0_x = fitpara_x(4);

N_x = fitpara_x(5);

sig_x(scan,imNo) = sig0_x*(pi/2).^(2/fitpara_x(5)-1);

% Get the fit parameters of y profile

base_y = fitpara_y(1);

amplitude_y = fitpara_y(2);

peak_center_y = fitpara_y(3);

sig0_y = fitpara_y(4);

N_y = fitpara_y(5);

sig_y(scan,imNo) = sig0_y*(pi/2).^(2/fitpara_y(5)-1);


% Printing out parameters to check.

string_x = [

    num2str(I(scan),'  %2.2f'),'     ', ...

    num2str(imNo,'%d'),'       ', ...

    num2str(base_x,'%12.2f'),'      ', ...

    num2str(amplitude_x,'%12.f'),'          ', ...

    num2str(peak_center_x,'%12.2f'),'        ', ...

    num2str(N_x,'%12.4f'),'     ', ...

    num2str(sig0_x,'%12.2f'),'        ', ...

    num2str(sig_x(scan,imNo),'%12.2f'),'     ', ...

    ];

%disp(string_x);

string_y = [

    num2str(I(scan),'  %2.2f'),'      ', ...
```

```
        num2str(imNo,'%d'),'           ', ...
        num2str(base_y,'%12.2f'),'          ', ...
        num2str(amplitude_y,'%12.f'),'             ', ...
        num2str(peak_center_y,'%12.2f'),'          ', ...
        num2str(N_y,'%12.4f'),'       ', ...
        num2str(sig0_y,'%12.2f'),'          ', ...
        num2str(sig_y(scan,imNo),'%12.2f'),'       ', ...
        ];
%disp(string_y);
%sig


% Plot to check.
%plot(x,profx,'k');
%hold on;
%plot(y,profy,'k');
%hold on;



% Construct fit curve from the fit parameters.
y_fit_x = fitpara_x(1)+fitpara_x(2)*exp( -0.5*(abs(x-fitpara_x(3))/
(fitpara_x(4))).^fitpara_x(5) );
y_fit_y = fitpara_y(1)+fitpara_y(2)*exp( -0.5*(abs(y-fitpara_y(3))/
(fitpara_y(4))).^fitpara_y(5) );


%plot(x,y_fit_x,'r');


%plot(y,y_fit_y,'r');
drawnow
```

```matlab
end
end

for scan=1:scan_current_number

% Find mean and standar deviation.
sig_mean_x(scan) = mean(sig_x(scan,:));
sig_mean_y(scan) = mean(sig_y(scan,:));
sig_x_er(scan)   = std(sig_x(scan,:));
sig_y_er(scan)   = std(sig_y(scan,:));

% Converting from pixels to length (in m unit).
sig_mean_x(scan)=sig_mean_x(scan)*calibration_x; %
sig_mean_y(scan)=sig_mean_y(scan)*calibration_y; %
sig_x_er(scan)= sqrt((sig_x_er(scan)*calibration_x).^2+(sig_mean_x(scan)*
er_calibration_x).^2);
sig_y_er(scan)= sqrt((sig_y_er(scan)*calibration_y).^2+(sig_mean_y(scan)*
er_calibration_y).^2);

% Squared sigma.
sig_sqr_x(scan) = sig_mean_x(scan)*sig_mean_x(scan);
sig_sqr_x_er(scan) = 2*sig_mean_x(scan)*sig_x_er(scan);
sig_sqr_y(scan) = sig_mean_y(scan)*sig_mean_y(scan);
sig_sqr_y_er(scan) = 2*sig_mean_y(scan)*sig_y_er(scan);


%I(scan) = I_start + (scan-1)*I_increment;
%plot(I,sig_mean,'r');
```

```
%Get the quarupole strength and its error from the dipole current.
k1(scan) =0.2998*(3.6*0.0001+1945*0.000001*I(scan))/(0.0254*p);


k1_Er(1) =0.2998*((3.6+1.3)*0.0001+(1945+2)*0.000001*I(scan))/(0.0254*p);
k1_Er(2) =0.2998*((3.6-1.3)*0.0001+(1945+2)*0.000001*I(scan))/(0.0254*p);
k1_Er(3) =0.2998*((3.6+1.3)*0.0001+(1945-2)*0.000001*I(scan))/(0.0254*p);
k1_Er(4) =0.2998*((3.6-1.3)*0.0001+(1945-2)*0.000001*I(scan))/(0.0254*p);
er_k1(1)=abs(k1(scan)-k1_Er(1));
er_k1(2)=abs(k1(scan)-k1_Er(2));
er_k1(3)=abs(k1(scan)-k1_Er(3));
er_k1(4)=abs(k1(scan)-k1_Er(4));


k1_er(scan)=max(er_k1);


k1L(scan) = L_ef(scan)*k1(scan); %k1*L
er_k1L(scan) = sqrt((L_ef(scan)*k1_er(scan) )^2+(Er_L_ef(scan)*k1(scan))^2);
%er_k1L(scan) = L_ef*k1_er(scan);


% Put the parameters together to pass to parabolic fits
FitDatX = [k1L',er_k1L',sig_sqr_x',sig_sqr_x_er'];
FitDatY = [k1L',er_k1L',sig_sqr_y',sig_sqr_y_er'];


end


 X_fit_data = fopen('X_fit_data.txt','w');
 Y_fit_data = fopen('Y_fit_data.txt','w');
 %fprintf(X_fit_data,'%4f %4f %4f %4f \n',k1L(16:31)',er_k1L(16:31)',
 sig_sqr_x(16:31)*10^6',sig_sqr_x_er(16:31)*10^6');
```

```
%fprintf(Y_fit_data,'%4f %4f %4f %4f \n',k1L(2:15)',er_k1L(2:15)',
sig_sqr_y(2:15)*10^6', sig_sqr_y_er(2:15)*10^6');
fprintf(X_fit_data,'%4f %4f %4f \n',k1L(16:31)', sig_sqr_x(16:31)'*10^6,
sig_sqr_x_er(16:31)'*10^6);
fprintf(Y_fit_data,'%4f %4f %4f \n',k1L(2:15)', sig_sqr_y(2:15)'*10^6,
sig_sqr_y_er(2:15)'*10^6);
fclose(X_fit_data);
fclose(Y_fit_data);

% Converting to cgs (mm and mrad) units.
 [k1L(16:31)' sig_sqr_x(16:31)'*10^6 sig_sqr_x_er(16:31)'*10^6]
 [k1L(2:15)' sig_sqr_y(2:15)'*10^6 sig_sqr_y_er(2:15)'*10^6]

%Emit_Parabola_Fit_kl_XProjection(k1L,er_k1L,sig_sqr_x,sig_sqr_x_er,me,En,
S12,erS12,scan_current_number);
%Emit_Parabola_Fit_kl_YProjection(k1L,er_k1L,sig_sqr_y,sig_sqr_y_er,me,En,
S12,erS12,scan_current_number);
Emit_Parabola_Fit_kl_XProjection(k1L(16:31),er_k1L(16:31),
sig_sqr_x(16:31)*10^6,sig_sqr_x_er(16:31)*10^6,me,En,En_er,S12,erS12,16);
Emit_Parabola_Fit_kl_YProjection(k1L(2:15) ,er_k1L(2:15),
sig_sqr_y(2:15)*10^6, sig_sqr_y_er(2:15)*10^6, me,En,En_er,S12,erS12,14);
```

B.2   Super Gaussian Fit

`SupGau_devsum.m`

function is being called during by

`Emit_Calc.m`

to fit super Gaussian to beam transverse profile.

```
function chisq = SupGau_devsum(a,X,Y)
% a(1) = base
% a(2) = A;   %amplitude
% a(3) = x0; %center
% a(4) = D;   %sigma_0
% a(5) = N;   %N=2 is nomal Guassian.
             %N<super Gaussian (sharp top).
             %N>Flat top shape Gaussian.
SupGau = a(1)+a(2)*exp( -0.5*(abs(X-a(3))/(a(4))).^a(5) ); % super Gaussian
csq = (Y - SupGau).^2;
chisq = sum(csq);
return
```

B.3   Parabolic Fit

```
Emit_Parabola_Fit_kl_XProjection
```

fits parabola for given rms values, plots the fit and extract emittance from the fit.

```
function varargout = Emit_Parabola_Fit_kl_XProjection(x,erx,y,ery,me,En,
En_er,S12,erS12,NumPoints)

%x
%y
%ery

order = 2; % second order fit
ParNum = order + 1;
```

```
% finding row matrix beta
for k=1:ParNum
for i=1:NumPoints
    f(k)=power(x(i),k-1);
    %fprintf('   i=%d  f(%d)=%g \t',i,k,f(k));
    beta_element(k,i)=y(i)*f(k)/(ery(i)*ery(i));
    %fprintf('y(i=%d)=%g ery(i=%d)=%g \n',i,y(i),i,ery(i));
    %fprintf('beta(k=%d,i=%d)=%g \n',k,i,beta_element(k,i));
    beta(k)=sum(beta_element(k,:));
    %fprintf('beta_element(%d,%d)=%g
    %beta(%d)=%g\n',k,i,beta_element(k,i),k,beta(k));
end
end
%beta

% finding matrix alpha
for k=1:ParNum
for l=1:ParNum
    for i=1:NumPoints
        f(k)=power(x(i),k-1);
        f(l)=power(x(i),l-1);
        alpha_element(k,l,i)=f(k)*f(l)/(ery(i)*ery(i));
        alpha(k,l)=sum(alpha_element(k,l,:));
        %fprintf('alpha_element(%d,%d,%d)=%g alpha(%d,%d)=%g\n',k,l,i,
        alpha_element(k,l,i),k,l,alpha(k,l));
    end
end
```

```matlab
end
%alpha


%To find fit parameters, need to invert matrix alpha.
alpha_invert = inv(alpha);
%alpha_invert


% The fit is y = a(1) + a(2)*x + a(3)*x*x
%fit parameters by matrix inversion method
parameter = beta*alpha_invert; %a(1)=parameter(1)
%parameters
fit_m_inver = parameter(1) + parameter(2)*x + parameter(3)*x.*x;
% error on the parameters
er_a = sqrt(diag(alpha_invert));


%fit parameters by MatLab
par = polyfit(x,y,2);
%par
fit_MatLab = par(3) + par(2)*x + par(1)*x.*x;


%Get Emittance and Twiss parameters from fit
gamma = En/me;
er_gamma = En_er/me;
beta = sqrt(1-1/gamma^2);
er_beta = er_gamma/(gamma^3*beta);


A=parameter(3);
B=-parameter(2)/(2*A);
```

```
C=parameter(1)-A*B^2;
erA = er_a(3);
erB = sqrt( (-er_a(2)/(2*A))^2 + (parameter(2)*erA/(2*A^2))^2 );
erC = sqrt((er_a(1))^2 + (-B^2*erA)^2 + (-2*A*B*erB)^2);
%fprintf('A=%g+-%g  B=%g+-%g  C=%g+-%g\n',A,erA,B,erB,C,erC);


emit = sqrt(A*C)/((S12)^2);
er_emit = sqrt( (1/2*A^(-1/2)*A^(1/2)*erA/(S12)^2)^2 +
(1/2*A^(1/2)*A^(-1/2)*erC/(S12)^2)^2 + ( 2*sqrt(A*C)*erS12/(S12)^3)^2 );
emit_n = emit*gamma;
er_emit_n = sqrt((emit*er_gamma*beta)^2+(emit*gamma*er_beta)^2+
(er_emit*gamma*beta)^2);
beta_func = sqrt(A/C);
er_beta_func = sqrt( (1/2*sqrt(1/(A*C))*erA)^2 + (-1/2*sqrt(A/C^3)*erC)^2 );
alpha_func = beta_func*(B + 1/S12);%alpha_func = sqrt(A/C)*(B + 1/S12)
er_alpha_func = sqrt(((B+1/S12)*er_beta_func)^2 + (beta_func*erB)^2 +
(-beta_func*erS12/(S12)^2)^2 );


figure(1)


set(axes,'FontSize',40)
pardat = errorbar(x,y,ery,'MarkerSize',30,'Marker','.','LineStyle','none',...
'LineWidth',3,...
'DisplayName','Data Points',...
'Color',[0 0 1]);
hold on


%Plot fit done by matrix inversion method.
```

```
parfit_m_inver = plot(x,fit_m_inver,'r');
set(parfit_m_inver,'LineWidth',3);


legend('Data','Fit');
set(legend,'Position',[0.73 0.75 0.1 0.1]);
set(legend,'FontSize',40);
set(legend,'FontName','Times New Roman');


hx = xlabel('k_{1}L (m^{-1})','FontSize',48,'FontName','Times New Roman');
hy = ylabel('\sigma^2_x (mm^2)','FontSize',48,'FontName','Times New Roman');
box off; % remove the top and right axes


%set(gca,'ticklength',4*get(gca,'ticklength'));
set(gca,'ticklength',[0.06 0.9]);
fit=title('');
%fit=title('15.6 MeV, X-Projection: k_{1}L vs \sigma^2');
set(fit,'FontSize',24,'FontWeight','bold','FontName','Times New Roman');
axis([-0.05 0.55 2.3 3.2]); %axis([xmin xmax ymin ymax])
%axis('FontSize',28);


saveas(fit,'Emit_Calc_plots\par_fit_x.fig','fig');
saveas(fit,'Emit_Calc_plots\par_fit_x.eps','epsc');
saveas(fit,'C:\Users\sadiq\Desktop\IPAC12\Paper\par_fit_x.eps','epsc');
saveas(fit,'Emit_Calc_plots\par_fit_x.png','png');
drawnow


fprintf('x-projection:\n\nemit=%.3f +- %.3f mm*mrad, emit_norm=%.2f +-
%.2f mm*mrad \n\n', emit, er_emit, emit_n, er_emit_n);
```

```
fprintf('beta=%.2f +- %.2f m, alpha=%.2f +- %.2f rad \n\n', beta_func,
er_beta_func, alpha_func, er_alpha_func);
fprintf('parabola fit for y-projection (y in mm unit): \n y = (%.5f +-%.5f)
+ (%.5f+-%.5f)*x + (%.5f+-%.5f)*x.*x \n\n', parameter(1),er_a(1),
parameter(2),er_a(2), parameter(3),er_a(3));
return
```

References

[1] S., Chemerisov. and C. D., Jonah, "Generation of high intensity thermal positron beams using a 20-MeV electron linac," *INTERNATIONAL WORKSHOP ON POSITRONS AT JEFFERSON LAB*, Newport News, Virginia, 2009.

[2] North Carolina State University, *http://www.ne.ncsu.edu/nrp/ips.html*, Intense Positron Beam, Nuclear Reactor Program, 2013-06-28.

[3] M. N. Rosenbluth, *Phys. Rev.*, 18, 1014 (1950).

[4] R. C.Walker *et al.*, *Phys. Rev. D*, 49, 5671 (1994).

[5] J. Arrington, *Phys. Rev. C*, 68, 034325 (2003).

[6] R. C. Walker, *Ph.D. thesis*, California Institute of Technology, 1989.

[7] H.W. Koch & J.W Motz, *Rev. Mod. Phys.*, 31, 920 (1959).

[8] K. S. Krane, *Introductory Nuclear Physics*, John Wiley & Sons, New York, 1988.

[9] NIST, *http://physics.nist.gov/cgi-bin/Xcom/xcom2*, NIST XCOM, 2013-05-03.

[10] M. Conte, & W. W. Mackay, *An Introduction To The Physics Of Particle Accelerators*, World Scientific, New York, 2008.

[11] V.L Ginzburg & I.M. Frank, *Sov. Phys. JETP*, 16, 15 (1964).

[12] B. Gitter, Tech. Rep., Los Angeles, USA (1992).

[13] K.T. McDonald and D.P. Russell, Fron. of Par. Beams Obser. Diag. and Cor. **08544**, (1988).

[14] Y. Kim *et al.*, in *Proc. FEL*2008, Gyeongju, Korea.

[15] D.F.G. Benedetti, *et al.*, Tech. Rep., DAFNE Tech. Not., Frascati, Italy (2005).

[16] S.Y. Lee, *Accelerator Physics*, (Singapore: World Scientific, 2004), 61.

[17] F.J. Decker, NASA STI/Recon Tech. Rep. N **1994**.

[18] Muons, Inc., *http://public.muonsinc.com/*, 2013-08-08.

[19] CERN, *http://geant4.cern.ch/*, 2013-08-08.

[20] B. KC & Y. Kim, *http://www2.cose.isu.edu/-yjkim/course/2010fall/2010fall-ap-term-project06.pdf*, ISU Phys. Dept., 2013-05-26.

[21] SAINT-GOBIAN, *http://www.detectors.saint-gobain.com*, SAINT-GOBIAN CRYS-TALS Technical Information Notes, 2013-06-11.